POLITECNICO
MILANO 1863

RE.PUBLIC@POLIMI
Research Publications at Politecnico di Milano

Post-Print

This is the accepted version of:

P. Panicucci, F. Ornati, F. Topputo
Design of a Low-Aberration Variable-Magnification Optical Stimulator for Vision System Hardware-in-The-Loop Testing
IEEE Transactions on Aerospace and Electronic Systems, Vol. 61, N. 6, p. 15224-15243, 2025 (published online 17/06/2025)
doi:10.1109/TAES.2025.3580393

The final publication is available at https://doi.org/10.1109/TAES.2025.3580393

Access to the published version may require subscription.

When citing this work, cite the original published paper.

© 2025 IEEE. Personal use of this material is permitted. Permission from IEEE must be obtained for all other uses, in any current or future media, including reprinting/republishing this material for advertising or promotional purposes, creating new collective works, for resale or redistribution to servers or lists, or reuse of any copyrighted component of this work in other works.

Permanent link to this version
http://hdl.handle.net/11311/1292723

Design of a low-aberration variable-magnification optical stimulator for vision system hardware-in-the-loop testing

Paolo Panicucci
Department of Aerospace Science and Technology, Politecnico di Milano

Fabio Ornati
Department of Aerospace Science and Technology, Politecnico di Milano

Francesco Topputo
Department of Aerospace Science and Technology, Politecnico di Milano

***Abstract*— The increasing interest in spacecraft autonomy raises the need for a trustworthy approach to perform Verification & Validation. In particular, vision-based navigation algorithms have established themselves as effective solutions to determine the spacecraft state in autonomy, with low-cost and versatile sensors. Nevertheless, thorough testing must be performed on ground to understand the algorithm robustness and performance in flight. A dedicated simulation framework must be developed to emulate the orbital environment in a laboratory setup. This paper presents a methodology to design and develop a low-aberration optical facility for visual sensors. The proposed methodology foresees two steps. First, a preliminary design is performed to identify the range of possible components to use in the facility according to the requirements. Then, a detailed optical design is performed to optimize the number and properties of the lenses composing the optical systems. The final design is compared against the preliminary one to show the superiority of the optical performance achieved with this approach. The proposed methodology is exploited to design and integrate a physical facility able to accommodate cameras with different characteristics (e.g., sensor size and focal length) while ensuring accurate stimulation. Besides these results, this work also presents a subpixel-accuracy geometrical calibration procedure to correct the geometrical errors due to component centering and misalignment. The estimated calibration is pivotal to compensating residual geometrical errors, enabling the stimulation of the camera at tens of arcseconds accuracy. Finally, two applications are presented to show the versatility of the developed setup in accommodating different cameras and in simulating heterogeneous mission scenarios.**

I. Introduction

Current space missions foresee complex and risky operations. In-orbit servicing, landing, or surface activities will soon become routine, pushing the need for spacecraft autonomy. These tasks cannot be performed with human-in-the-loop operations, as communication delays could lead to catastrophic failures. The spacecraft needs to be reactive and aware of environmental changes to fulfill mission objectives. Moreover, the current ground-based communications can only operate a limited number of probes with considerable costs. The increasing number of planned missions raises concerns on the sustainability of operating a multitude of spacecraft. Increasing autonomy is one of the most appealing solutions to solve these issues. This requires developing algorithms and methods to enhance spacecraft with autonomous capabilities. All in all, the spacecraft must be able to sense the external environment, decode the sensor measurements, and gather its state within the environment. One of the solutions to achieve these goals is vision-based navigation (VBN). Indeed, cameras marginally affect the spacecraft mass, power, and size budgets, resulting in being the preferred alternative with respect to other costly and massive sensors (such as LiDAR). Moreover, image processing algorithms can achieve subpixel accuracy, resulting in precise and real-time measurements for navigation filters. In addition, VBN has proven to be versatile in all mission phases: cruise [1, 2, 3], approach [4, 5, 6], mid-range [7, 8, 9], and close proximity [10, 11, 12, 13].

These advantages come a cost. A crucial step is the Validation and Verification (V&V) of the VBN algorithm. Testing on orbit is extremely costly, even when the algorithm has a high Technology Readiness Level (TRL). The absence of in-orbit testing leads to high risks in the final product, increasing costs when issues arise at late-stage development. Because of this reason, on-ground testing is exploited to assess the correct deployment, integration, and performance of vision-based systems. Current approaches rely on the generation of realistic datasets to assess the algorithm performance and the computation burden on hardware components. In the context of complex spacecraft operations (e.g., on-orbit servicing and space exploration), it is hard to collect image datasets from previous missions. Therefore, V&V of the VBN chain is assessed incrementally, by tackling a single feature individually in validation environments of increasing complexity. First, numerical simulations are performed by simulating cameras with dedicated rendering engines, such as ESA's PANGU [14] or Airbus Defence & Space's SurRender [15]. Second, processor-in-the-loop (PIL) simulations are performed to assess the algorithm execution and latency on representative hardware. Finally, camera-in-the-loop (CIL) simulations are put in

This research is part of EXTREMA, a project that has received funding from the European Research Council (ERC) under the European Union's Horizon 2020 research and innovation programme (Grant Agreement No. 864697). *(Corresponding author: P. Panicucci).*

All authors are with the Department of Aerospace Science and Technology, Politecnico di Milano, Via La Masa, 34, 20156 Milano, Italy (e-mails: paolo.panicucci@polimi.it, fabio.ornati@polimi.it, and francesco.topputo@polimi.it).

place to understand the image processing performance in the presence of the optical system distortions and aberrations, which could degrade the VBN estimates.

Performing validation tests in experimental laboratories is a complex task. The camera is a geometrical and radiometric sensor, implying that it must observe the scene from a specific point of view with a light signal equivalent to the one received in orbit. To do so, CIL testing is performed in two different test-benches: optical and robotic facilities. The former consists of a screen stimulating the camera via a lens system. These facilities still rely on image generation, but their development and maintenance costs are limited. Conversely, the latter comprises robotic components moving the sensor and a target mock-up to mimic the observational scenario. These facilities generate realistic images as light physically propagates from the target to the detector, but they are costly and complex to operate. In algorithm testing, their complementary and incremental use overcome both limitations and increase the validation realism. Optical facilities are usually used to preliminary assess the algorithm robustness before moving to more complex and costly robotic facility testing.

This work aims to present a methodology to design and develop a low-aberration optical facility. After the theoretical design, this work focuses on the optical performance and its optimization. The low-aberration facility designed with this approach is capable of accommodating cameras with different optical head and detector characteristics. This versatility results in ensuring light collimation with a reduced level of chromatic and achromatic aberrations during testing. The design approach enables using of different cameras thanks to its two-lens-assembly design that ensures variable magnification of the screen image. Moreover, the lens assemblies are designed with commercial-of-the-shelf (COTS) components optimized to reduce the chromatic and achromatic aberration due to the multi-lens design. Finally, a dedicated geometrical calibration algorithm is designed to achieve sub-pixel precision and accuracy to compensate for errors due to residual distortions and misalignment. These hardware and software components ensure that the camera mounted in the optical stimulator can observe the scene projected on the screen to correctly assess the VBN chain performance with the camera in the simulation loop. The paper presents analyses and results by focusing on the DART Lab's RETINA (Realistic Experimental faciliTy for vIsion-based NAvigation), yet the developed techniques can be exploited for other test-benches.

The remainder of the paper is organized as follows. Section II summarizes the notation used in this work. Section III presents the state of the art for optical stimulators. Section IV gives an overview of facility components and their integration. Section V discusses the requirements for facility constraints, focusing on the design methodology. Section VI details the geometrical calibration procedure devised to ensure arcsecond accuracy in the stimulation. Section VII presents the results obtained in testing two algorithms in RETINA. Finally, Section VIII summarizes the main findings of this work.

II. Notation

In this document, the following notation is used:

- 3D and 2D vectors are denoted respectively with lower and upper case bold text, such as $\boldsymbol{r}$ and $\boldsymbol{R}$.
- Matrices are in plain text in brackets, such as $[A]$.
- Vector initialization is performed with parenthesis, such as $\boldsymbol{b} = \left(\boldsymbol{a}^T\ \boldsymbol{a}^T\right)^T$.
- $\mathcal{A} = \{a, \boldsymbol{a}_1, \boldsymbol{a}_2, \boldsymbol{a}_3\}$ is the 3D reference frame centered in the 3D point a with axes $\boldsymbol{a}_1$, $\boldsymbol{a}_2$, and $\boldsymbol{a}_3$. All the reference frames are right-handed and orthonormal.
- The rotation matrix from $\mathcal{S}$ to $\mathcal{C}$ is $[CS]$. All rotations are treated as passive (i.e., frames are rotated, rather than vectors [16]).
- $\mathbb{A} = \{A, \boldsymbol{A}_1, \boldsymbol{A}_2\}$ is the a 2D reference frame centered in the 2D point A with axes $\boldsymbol{A}_1$ and $\boldsymbol{A}_2$ which are orthonormal.
- The 3D vector $\boldsymbol{r}$ in homogeneous form is labeled ${}_h\boldsymbol{r}$ and the 2D vector $\boldsymbol{R}$ in homogeneous form is labeled ${}_h\boldsymbol{R}$.
- The projection of the 3D vector $\boldsymbol{r}$ on the 2D image is labeled $\boldsymbol{R}$.

III. Background on Hardware-In-the-Loop Optical Facility

Optical facilities were designed in the past to assess the star tracker performance on ground [17, 18, 19, 20, 21]. The first work in the literature reporting the development and the use of an optical facility is Rufino and Moccia [22], which presents the design of an optical facility composed of a cathode ray tube display stimulating a star tracker through a collimator. This work analyzes the geometrical and radiometrical requirements the component must fulfill to enable the correct star tracker stimulation. Moreover, the analytical performance attainable in this category of facilities is initially reported in Rufino and Moccia [22] and investigated in more detail in Rufino and Moccia [17]. A similar design with more recent technology is reported in Rufino et al. [18] where the cathode ray tube display is substituted with an LCD screen. In these works, the geometrical calibration of the facility is obtained by estimating the misalignment and the optics distortion with neural network [23], while the radiometric calibration is obtained by exploiting the knowledge of the screen mapping from illuminance to digital number (DN) thanks to calibration curves provided by the manufacturer [17, 18, 22].

A similar design is presented in Filipe et al. [19] to test the ADCS subsystem of the MarCO and ASTERIA CubeSats. To perform this test, the facility was accommodated on an air-bearing system to perform closed-loop ADCS simulations. Therefore, Filipe et al. [19] focuses on the miniaturization of the facility thanks to an OLED smartphone display mounted at the end of a rigid bar. This enables stimulating the camera mounted on the air-bearing system with collimated light while reaction wheels control the platform. The facility is geometrically calibrated, but not radiometrically. Indeed, the work details a procedure to tackle the problem of radiometric calibration, but the detailed method does not achieve satisfactory results as the assumption of a linear map between DN and illuminance does not hold.

For larger star trackers, Jena-Optronik's Optical Sky field sImulator (OSI) [20] and MINISTAR [21] were designed to test hardware after integration of the components on the spacecraft. The test benches are geometrically calibrated to correctly stimulate the camera with a miniaturized OLED microdisplay through a collimator. OSI is radiometrically calibrated by the manufacturer, while no information is available about the radiometric calibration procedure for MINISTAR.

Recent interest in autonomous vision-based navigation (VBN) and the need for their validation have motivated the application of optical facilities to vision-based systems [24, 25, 26, 27]. Roessler et al. [24] presents an optical test bench similar to the one outlined in Rufino et al. [18], but it is used in the context of spacecraft rendevous VBN algorithm validation. The facility is geometrically calibrated by compensating the facility-induced errors with an estimated homography. Stanford's SLAB also developed its facility to test the developed vision-based algorithms [25, 26]. Beierle et al. [25, 26] present a radiometrically and geometrically calibrated design to test autonomous formation flight navigation. The design is a collimated single-lens system where an OLED microdisplay is used to stimulate the camera. The radiometric calibration is performed by measuring the mapping between the screen DN and the displayed celestial object irradiance via a power meter. Moreover, the geometrical calibration is performed by fitting a high-order polynomial to compensate for both misalignments and distortions induced by the facility. The obtained facility can display celestial objects with a wide range of irradiance with a projection error of less than tens of arcseconds. An improved design is presented in Beierle and D'Amico [28] where a double-lens system is exploited to obtain variable magnification of the facility. This variable magnification implies that cameras with different FoVs can be tested with the same facility simply by regulating the relative distance between the lenses. These improvements come at the cost of a more complex optical design inducing high distortions and aberrations. To the authors' understanding, the facility design includes two cemented achromatic doublets to magnify the screen image to fit the screen height with the camera FoV. It is worth mentioning that this facility has been recently used to validate on-ground autonomous vision-based navigation for formation flight [29].

A single-lens collimated design is also presented in Panicucci and Topputo [27] where the facility is designed to test space exploration scenarios (e.g. deep-space and asteroid navigation). In this work, geometrical calibration is addressed by presenting two different approaches to compensate for facility-induced errors: upstream and downstream compensations. In the former, errors are compensated before projecting the image on the screen, while the latter approach compensates errors after the camera acquisitions induced by the hardware-in-the-loop (HIL) testing. In both cases, the compensation is achieved by using a high-order polynomial to fit the facility-induced distortions. The radiometric calibration is not presented in Panicucci and Topputo [27] even though detailed in Andreis et al. [30].

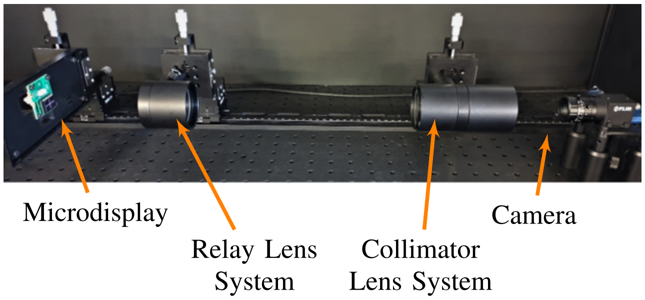

Fig. 1: The physical realization of the low-aberration variable-magnification facility proposed in this work.

In this context, this work aims to present the design of a two-lens optical stimulator with variable magnification. The proposed stimulator differs from the previous design because its optical design is optimized to show superior optical performance thanks to optimized lens systems. The physical realization of this facility is RETINA, a HIL optical stimulator used to test image processing and vision-based navigation algorithms.

A summary of state-of-the-art optical facilities is reported in Table I for the sake of completeness.

IV. Overview of optical facility

The optical stimulator is designed to test and validate vision-based navigation algorithms in hardware-in-the-loop simulations to emulate the sensor condition in orbit. When mounted in the facility, spaceborne cameras are stimulated with limited distortion and aberration effects. To achieve so, the stimulator is designed with optimized hardware to correctly stimulate cameras with different FoV (i.e., sensor size and focal lengths). The high-level requirements on the facility state that the facility shall be compliant with FoV between 4 and 22 degrees. This range is selected as it is compatible with cameras used in DART Lab projects (e.g., LUMIO [34] and Milani [35]). Moreover, this range is compliant with the majority of space-graded hardware used for vision-based navigation, attitude determination, and scientific observations. The optical stimulator is composed of several components that are mounted on an optical breadboard and enclosed in a closed black box to limit external light pollution. For RETINA, the optical breadboard is 60 cm × 120 cm,

TABLE I: Summary of the optical facilities developed in the past for attitude and navigation testing.

	Radiometrically calibrated	Geometrically calibrated	Reduced optical aberrations	Variable magnification
UniNa Facilities [22, 17, 18]	✓	✓	NA[1]	✗
JPL Facilities [19]	✗	✓	NA[1]	✗
OSI [20]	✓	✓	NA[1]	✗
MINISTAR [21]	✗	✓	NA[1]	✗
UniDenmark Facilities [24]	✗	✓	NA[1]	✗
TinyV3RSE [31, 27, 32]	✓[2]	✓	NA[1]	✗
Stanford Single-lens Facility [25, 26]	✓	✓	NA[1]	✗
Stanford Two-lens Facility [28]	✓	✓	✗	✓[3]
RETINA	✓[2]	✓	✓	✓[4]

[1] Not applicable as single lens design.

[2] RETINA and TinyV3RSE radiometric calibrations are not presented in this work. Preliminary results are available in Andreis et al. [30] and Ornati et al. [33].

[3] Variable magnification can also be achieved during the simulation thanks to motorized optical stages.

[4] Variable magnification can only be achieved before the calibration to match the camera mounted in the facility.

which is selected as a compromise between facility size and requirement fulfillment (see Section V. In detail, the components are:

1) A controllable OLED microdisplay.
2) A relay lens system that magnifies the screen to perfectly fit the camera FoV.
3) A collimator lens system that collimates the magnified screen to emulate space observations.
4) A camera that is stimulated by the screen through the two lens systems.

A picture of RETINA is reported in Figure 1 showing the different components of the facility.

To design the facility, it is necessary to fix one of the components between the screen and the lens systems. For RETINA, the screen is selected based on illumination and size considerations. The screen has a small size (i.e., 18.7 mm × 11.75 mm) to ensure a compact facility and a pixel pitch of 9.6 μm to enable the display of small objects. The resolution is 1920 × 1200 pixels ensuring to display small features and unresolved celestial objects in the camera field of view. Moreover, it relies on OLED technology, implying an extreme dynamic range between the low and high-illuminated pixels and the absence of backlight leakage for inactive pixels. This ensures high contrast between the illuminated celestial objects and the dark background. Moreover, it is worth noting that a high dynamic range is beneficial to display a space scene as celestial objects usually exhibit large variations in magnitude between faint stars and bright resolved objects. The screen is attached to a custom interface which is mounted to an opto-mechanical stage that can be regulated with millimeter precision. This stage, as the other ones in the facility, is mounted on a translational rail that enables the relative displacement of the components.

Two lens systems are present in the facility, having respectively a very precise scope. In this section, a qualitative description of these lens systems is provided. A more detailed analysis of the lens systems preliminary design is reported in Section V-A, while the detailed optical design is reported in Section V-C.

The collimating lens system aims at collimating the light that stimulates the camera to emulate space observations. Indeed, observed celestial objects are usually distant with respect to the camera, leading to the possibility of considering the light ray parallel when entering the camera pupil [28, 17]. The relay lens system is included to magnify the screen to simulate the presence of a smaller or larger screen in the facility to fit the camera FoV. In single-lens design, this is achieved by choosing the collimator focal length according to the camera FoV and the screen height. The main drawback of this approach is the necessity of changing - thus purchasing - a new collimator every time a new camera must mounted in the facility. Conversely, a single screen can be magnified in a two-lens configuration by adjusting the relative distance between the relay lens systems and the collimating lens system. This results in the possibility of using the same lenses for multiple cameras without any need to change the hardware. Sadly, it comes at the cost of distorting and aberrating the light stimuli arriving at the camera pupil when passing through multiple lenses. The two lens systems designed for RETINA are designed to enable variable magnification (thus variable camera FoV) while minimizing the light stimuli distortions and aberrations. Both lens systems are mounted on opto-mechanical stages enabling the alignment and centering of the lens systems with millimeter precision.

V. Facility Design and Constraints

In this section, the facility design is outlined by underlining the main drivers and constraints. First, a paraxial lens model is employed to understand the main driver for the facility design. Second, the envelope of the possible facility parameter is established to perform an informed selection of the facility components. Finally, a detailed optical design is performed to optimize the identified preliminary configuration.

A. The two-lens paraxial model

A simplified model for the facility is analyzed in this section to enable a preliminary design. To ease the calculations, the paraxial approximation is made. This is a classical assumption in geometrical optics and it has been already used in the past to design optical facilities [27, 28, 17]. Figure 2 shows the two-lens paraxial model that is employed in this section.

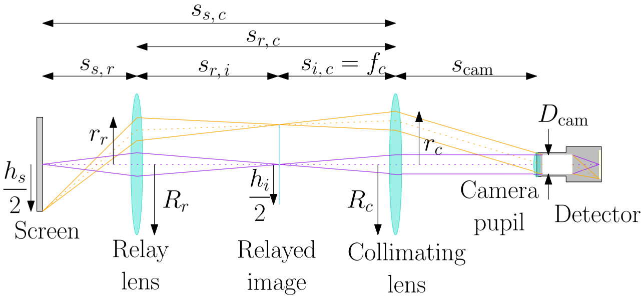

Fig. 2: The two-lens paraxial model used for the stimulator design.

The screen light passes through the relay lens generating the relayed image. The size of the relayed image can be computed as:

$$h_i = -M\,h_s \tag{1}$$

where h_i is the realy image height, h_s is the screen height, and M is the relay lens magnification. Note that the magnification M correlates with the distance between the screen and its image:

$$s_{r,\,i} = -M s_{s,\,r} \tag{2}$$

where $s_{s,\,r}$ is the distance between the screen and the relay lens and $s_{r,\,i}$ is the distance between the relay lens and the relayed image. Recall that the minus sign is justified by the fact that $M < 0$ as the generated image is a real one. To achieve this a convex lens is used as concave lenses always have a positive magnification factor as they generate virtual images.

As the light at the camera pupil must be collimated, the distance between the relayed image and the collimating lens $s_{i,\,c}$ is:

$$s_{i,\,c} = f_c \tag{3}$$

where f_c is the collimating lens focal length. This ensures that all the rays crossing the collimating lens are parallel. The optimal working condition of the facility occurs when the camera FoV observes the whole screen. As the relayed image is the magnification of the screen image, it is possible to match the relayed image size with the camera FoV as in single lens optical facilities [27, 17]:

$$h_i = 2 f_c \tan\left(\frac{\text{FoV}_{\text{cam}}}{2}\right) \tag{4}$$

where FoV_{cam} is the camera FoV. By using Equations 1 and 4, it is possible to compute the magnification factor associated with this condition:

$$M = -2\frac{f_c}{h_s}\tan\left(\frac{\text{FoV}_{\text{cam}}}{2}\right) \tag{5}$$

Equation 5 shows that it is possible to accommodate different cameras (i.e., FoV_{cam}) by changing the magnification level M, given the screen and the collimator (i.e., f_c and h_s).

Note that, by combining Equations 5 and 2, it is possible to find a relationship linking the component's location and the camera FoV:

$$\frac{s_{r,\,i}}{s_{s,\,r}} = 2\frac{f_c}{h_s}\tan\left(\frac{\text{FoV}_{\text{cam}}}{2}\right) \tag{6}$$

It is worth recalling that the screen and its image are linked by:

$$\frac{1}{f_r} = \frac{1}{s_{s,\,r}} + \frac{1}{s_{r,\,i}} \tag{7}$$

where f_r is the relay lens focal length. Thus, by using Equation 2:

$$s_{s,\,r} = \left(\frac{M-1}{M}\right) f_r \tag{8}$$

$$s_{r,\,i} = (1 - M)\, f_r \tag{9}$$

Equations 8 and 9 define the distance between the screen, the relay lens, and the relayed image. Indeed, by knowing the desired level of magnification M, the distance between the screen and the relay lens. Note that this also fixes the distance between the relay lens and the relayed image.

B. Feasible range of components parameters

From the paraxial model in Section V-A, it is possible to understand that three variables are driving the preliminary design of the facility: f_c, f_r, and h_s. It is worth noting that only one free parameter exists as the components properties are linked by Equations 6 and 7. As mentioned in Section IV, the RETINA's screen was selected among the ones available in the market for its illumination dynamical range, its reduced size, and its high frame rate (i.e., 60 Hz). This implies that the constraints given by Equations 6 and 7 define a range of feasible focal lengths to fulfill the facility requirements on the operative camera FoV. This section aims to present the methodology established to compute this feasible domain, to specialize it for RETINA, and to present the selected preliminary solution.

The first constraint to be taken into account is the total length of the rails where the opto-mechanical stages are mounted. The maximum distance between the components mounted in the facility is:

$$\begin{aligned} s_{s,\,c} =& s_{s,\,r} + s_{r,\,c} = s_{s,\,r} + s_{r,\,i} + s_{i,\,c} = \\ =& -f_r\left(\frac{1+M^2}{M}\right) + f_c \le s_{s,\,c}^{\max} \end{aligned} \tag{10}$$

where $s_{s,\,c}^{\max}$ is the maximum length. For RETINA, this length is 850 mm, given the breadboard length and the opto-mechanical stage size. Note that M is computed by Equation 5. This constraint is necessary to ensure that all components are correctly accommodated within the enclosing box and the correct movement of the stages on the transnational rail.

The second constraint to consider is the minimal allowed distance between the opto-mechanical stages. Indeed, owing to their physical size, it is not possible to approach two stages more than a given threshold $s_{r,\,c}^{\min} = s_{s,\,r}^{\min}$. Given the stages physical size, $s_{r,\,c}^{\min} = s_{s,\,r}^{\min} = 100$ mm for RETINA. Therefore:

$$(1 - M)\, f_r + f_c \leq s_{r,\,c}^{\min} \tag{11}$$

$$\left(\frac{M-1}{M}\right) f_r \leq s_{s,\,r}^{\min} \tag{12}$$

The last constraint relates to vignetting. Indeed, when observing through the lenses, all the rays entering the camera pupils must come from the screen. When some rays are not passing through both lenses, vignetting is present. When this happens, the camera does not receive all the rays emitted by the screen, leading to a loss of stimulation at the image border. An example of this effect is reported in Figure 3.

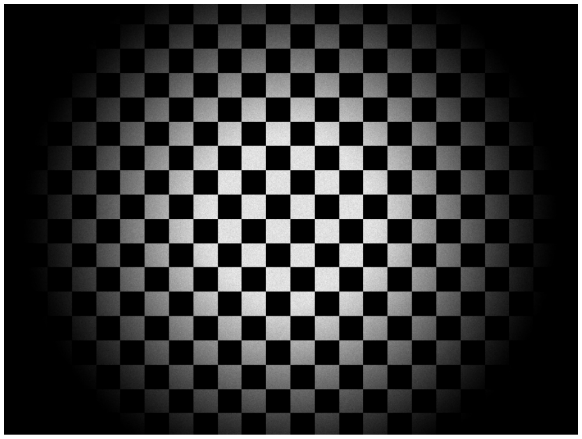

Fig. 3: An example of vignetting when the vignetting constraint is not verified.

To evaluate the effect of vignetting in the stimulation, a ray casting procedure is developed. Let R_r and R_c be the radius of the relay and the collimating lenses respectively. Let d_{cam} be the camera pupil as depicted in Figure 2. In the casting procedure, the rays having the same inclination of the camera FoV are considered as these are the outermost rays entering the camera pupil. These rays are the ones depicted in orange in Figure 2. These rays are cast through the paraxial model to compute their vertical intersection with the two lenses. The intersection with the collimating lens is labeled r_c, whereas the one with the relay lens is r_r. Note that, given a camera FoV, it is crucial to cast rays from the camera pupil limit to correctly assess vignetting as the intersection of the upper or lower ray could not be the extremal intersection with the lenses. No vignetting occurs when $r_r \leq R_r$ and $r_c \leq R_c$. When both conditions occur, the extremal rays of the camera FoV are correctly cast from the camera pupil to the screen. In RETINA's vignetting analyses, the camera pupil d_{cam} is set to 10 mm (i.e., F# = 1.2 for a 12 mm focal length optical head), and the distance between the camera pupil and the collimating lens (i.e., s_{cam}) is the optimal one for the considered camera FoV, given a combination of lenses radius (i.e., R_r and R_c) and focal lenses (i.e., f_r and f_c). To do so, before performing the vignetting analyses, a look-up table is computed for s_{cam} to be used in the vignetting analysis to assess the feasibility of a given FoV. Given the aforementioned constraints, a series of analyses are performed by varying f_c and f_r to understand which focal lenses can fulfill the FoV requirements. As the vignetting analysis is dependent on the lens radii as well, two different simulations were performed by considering that the collimating lens radius could assume the value of 1" or 0.5", which is compliant with COTS lens radii available on the market. Moreover, it is worth mentioning that cemented triplet lenses provide high performance against aberrations with reduced complexity in optical design. As these lenses are only available as COTS with a radius of 0.5", it is of interest to investigate a smaller relay lens radius. Note that the relay lens radius is fixed at 1" because a smaller lens radius would have been too stringent in terms of vignetting, providing no feasible solution.

The results of these analyses are shown in Figures 4a and 4b for R_c equal to 1" and 0.5" respectively. The black and brown areas are associated with unfeasible solutions due to the distances between the optical components. Indeed, too small focal lengths would imply small distances between components. The red area is associated with a total length greater than the maximum. This is associated with low relay lens focal lengths and small FoVs. Lastly, the blue area is associated with the vignetting effect. This effect limits the collimator focal lengths as the ideal image must be further away from the lens, leading to some rays not falling into the relay lens. The range of feasible solutions for the design is the not colored one which provides all the couples $(f_r,\, f_c)$ that are geometrically compliant with the constraints. Figure 4b shows a smaller range of feasible focal lengths, implying that a larger collimating lens radius gives more variability in the lens selection. Moreover, it is worth noting that for a greater camera pupil diameter, a small collimating lens diameter could imply the constant presence of vignetting. Therefore, RETINA was designed with $R_c = R_r = 1''$. Finally, the selected focal lengths must be located in the upper region of the feasible areas as higher focal lengths are preferred to achieve lower magnification errors when the components are not correctly placed in the facility [28].

C. Low-aberration optical design

In this section, the optical performance of RETINA preliminary design is studied. Then, the two lens systems are optimized to remove aberrations. To do so, a dedicated study in Zemax OpticStudio is performed as a simple paraxial model cannot predict the optical distortions and aberrations induced by the lenses mounted in the facility. The software is the state-of-the-art for optical design and analysis and it can compute the optical performance of

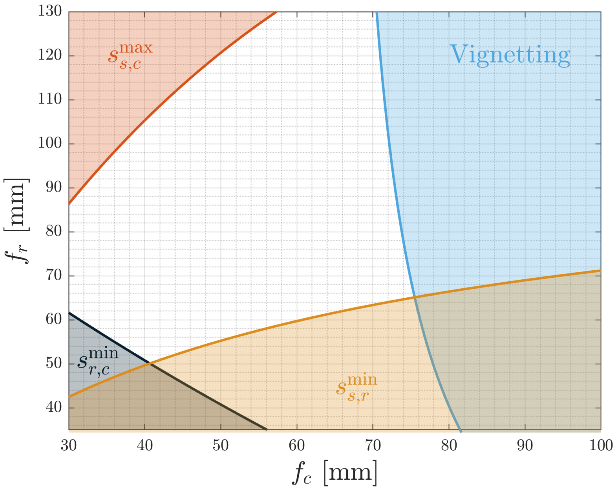

(a) $R_c = 1''$, $R_r = 1''$

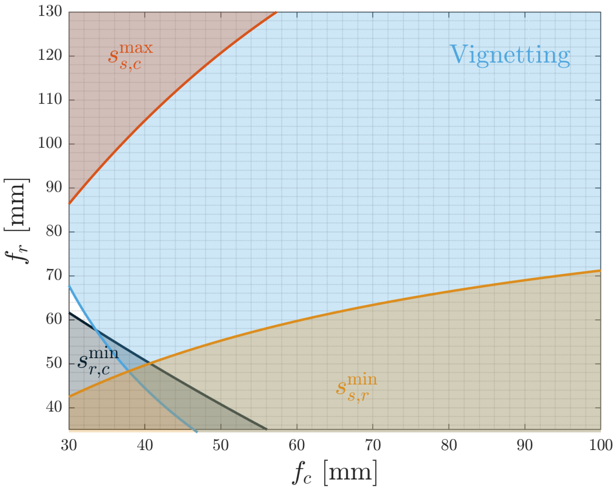

(b) $R_c = 0.5''$, $R_r = 1''$

Fig. 4: The range of feasible focal lengths for different values of lens radii.

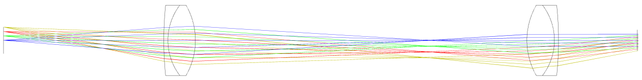

(a) 25-mm objective.

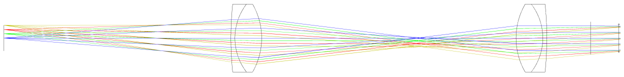

(b) 50-mm objective.

Fig. 5: Zemax sketch of the first investigated solution. Ray colors are associated with the screen-emitting height.

an optical system by sequential raytracing. As the optical design software requires the setting of the entrance camera pupil to compute the optical performance, the camera considered in this section has an F-number of 2.8. All the lenses considered in this section are COTS components to avoid cost increases and complex lens design. The lenses are modeled in Zemax according to their data-sheet characteristics to precisely assess the optical performance. Note that the use of COTS components makes optical performance optimization a challenging task as most of the optical systems optimize the lens characteristics (e.g., lens shape and curvature) to reduce optical aberrations. In the case of COTS components, this is not possible as the only design variable is the type of lens to be purchased and their relative distance. Therefore, several Zemax models have been implemented varying the number of lenses and their characteristics among the ones available on the market. For each Zemax model, an optimization has been performed to minimize the RMS radius (i.e., the root-mean-square value of the radius of all the rays generated from a single ray beam) of the optical system spot diagram to find the optimal distance between the lenses composing the relay and collimating systems.

This section will not detail all the iterative processes that led to the final solution, but it presents one of the first investigated solutions to show the importance of optical performance assessment. Then, the final configuration is presented.

The first investigated solution considers two 1”-radius achromatic cemented doublets with focal lengths of 75 mm. These lenses are selected as they reduce chromatic aberrations with a cemented double glass layer. In a preliminary investigation, also Hastings triplets were investigated owing to their superior optical performance, but they were discarded as their radius is 0.5” for COTS components (see Figures 4a and 4b). The Zemax model of this first iteration is reported in Figures 5a and 5b for an objective of 25 mm and 50 mm respectively. Note that these objectives are associated with extremal FoVs of the facility requirements.

On the left part of the model, the screen generates ray beams at different distances from the optical center to assess the optical response of the system. The collimator model is downloaded from the lens producer website and imported into the Zemax model. On the right part of the model, a paraxial objective was created to emulate the optical properties of a camera. This was done to evaluate the distortions and aberrations of the RETINA lens apparatus alone. The camera is devised with two lenses and an aperture stop to correctly fit the camera focal length and the camera pupil aperture. In Figures 5a and 5b, the ray beams are reported with different colors according to their distance with respect to the screen center for 25-mm and 50-mm objectives respectively. Each ray beam is propagated through the system to impact the camera sensor plane. This defines the spot diagram shown in Figures 6 and 7 where the spot color is associated with the ray wavelength (i.e., blue=486 nm, green=588 nm, and red=656 nm) for 25-mm and 50-mm objectives. In Figures 6 and 7 h_s is the point on the detector generating the spot diagram and α is the angular location associated with the center of the spot

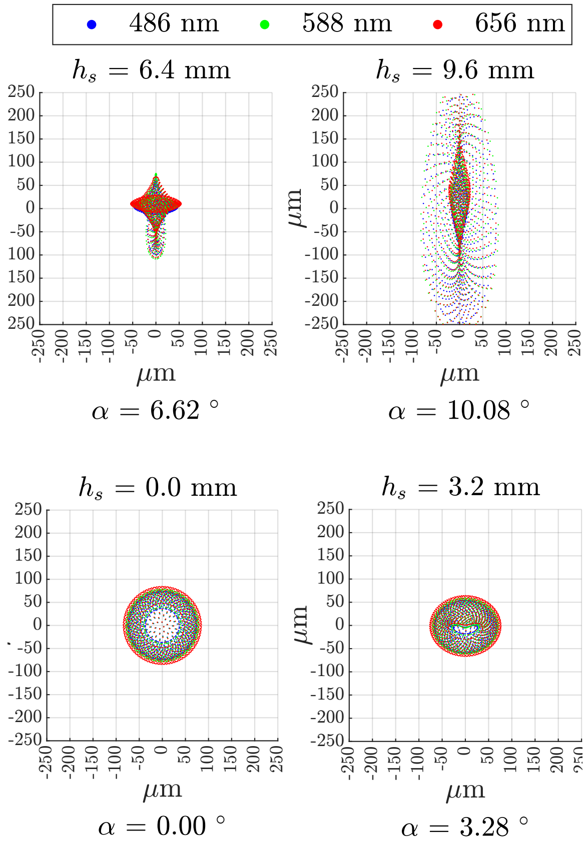

Fig. 6: Spot diagram of the model reported in Figures 5a and 5b for a 25-mm objective

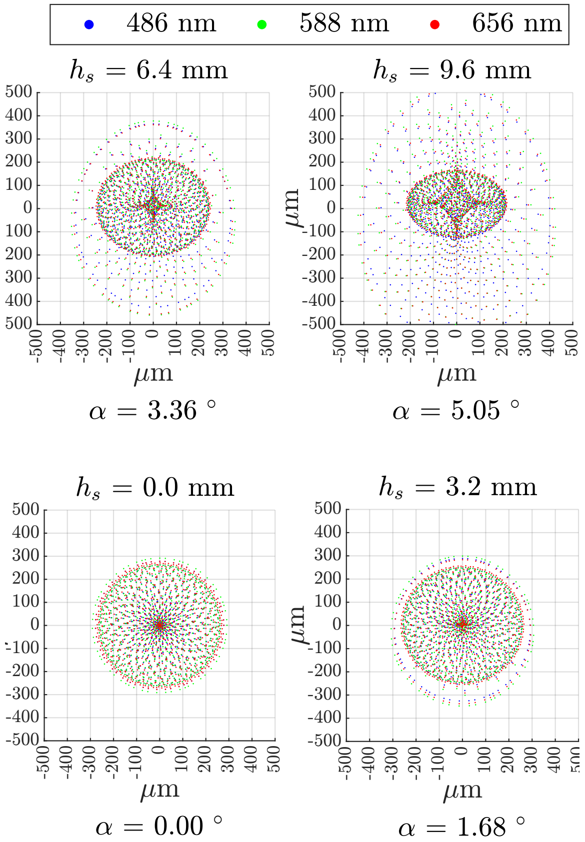

Fig. 7: Spot diagram of the model reported in Figures 5a and 5b for a 50-mm objective.

diagram. Note that the ray beam locations on the screen are selected to impact at different locations of the detector to account for variation of the performance in off-axis conditions. The numerical assessment of the simulation is reported in Table II where the RMS radius is provided in micrometer as a function of the distance from the detector center. The micrometer is chosen as camera pixels are usually of these order of magnitude, leading to an easy comparison according to the selected detector. It is possible to conclude that rays passing through the lenses close to the optical axis experience low aberrations and distortions, while the external ones show a very large degree of aberration. In particular, rays are extremely spread, leading to a severe blurring effect at the corner of the detector when observing the screen. An example of an image taken with this configuration is reported in Figure 8, proving experimentally the studied setup.

TABLE II: RMS radius of the spot diagram as a function of the detector position for the model reported in Figure 5

Camera Setup	Position on the screen [mm]	Position on the detector [mm]	Position in the FoV [deg]	RMS radius [μm]
25-mm objective	0	0	0	62.73
	3.2	1.43	3.27	50.63
	6.4	2.89	6.61	47.43
	9.6	4.41	10.08	128.34
50-mm objective	0	0	0	219.27
	3.2	1.47	1.68	224.31
	6.4	2.94	3.36	246.02
	9.6	4.41	5.05	298.93

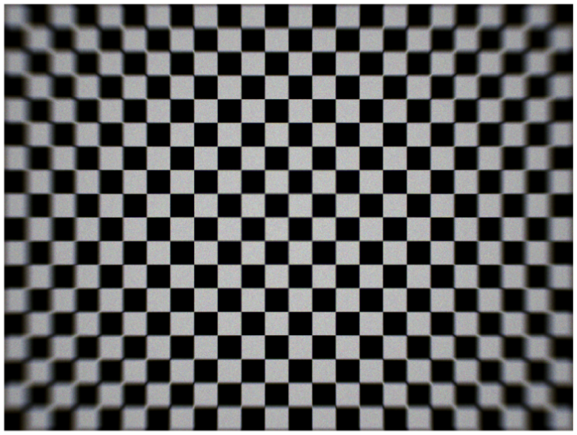

Fig. 8: An image of a regular pattern acquired in RETINA with the first investigated configuration.

In order to mitigate the aberrations and effects related to blurring, a different optical design must be put in place. As COTS components are used, it is not possible to optimize the lens shape and surface properties to minimize the aberrations induced by the collimating and relay lenses. A possible solution is to use a higher number of lenses, leading to an increase in degrees of freedom to increase the optical performance [36, 37]. Indeed, a higher number of lenses implies a higher number of distance to be optimized. It is worth recalling that a lens system composed of two lenses has an equivalent focal length f_{equiv} given by:

$$\frac{1}{f_{\text{equiv}}} = \frac{1}{f_1} + \frac{1}{f_2} - \frac{d}{f_1\, f_2} \tag{13}$$

where f_1 and f_2 are the focal lengths of the first and second lenses composing the lens system, and d is the distance between them. In the case of multiple lenses, Equation 13 can be used iteratively to compute the equivalent focal length. For both the collimating and relay lens systems the equivalent focal lengths must be compliant with the feasible ranges reported in Section V-B. This results in design constraints on the focal length of each single lens.

The selection of the number of lenses, their focal length, and their relative distance to ensure optical performance while ensuring the previous constraints is performed by Zemax simulations and iterations with the feasible ranges. The main drivers used in the selection process are:

1) The relay and collimating lens systems must not induce a high field curvature for the considered wavelengths (i.e., red, blue, and green) on the tangential and sagitial planes. This condition ensures that the screen image as seen from the camera is not warped too much during the propagation through the lens systems.
2) The equivalent single-lens focal lengths for both lens systems must be compliant with the feasible region in Figure 4a, with a preference for higher focal lengths.

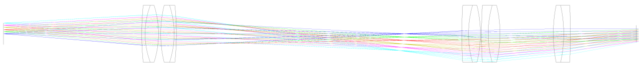

(a) 25-mm objective.

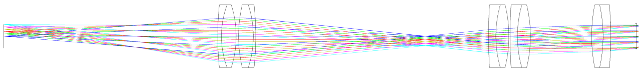

(b) 50-mm objective.

Fig. 9: Zemax sketch of the low-aberration investigated solution. Ray colors are associated with the screen-emitting height.

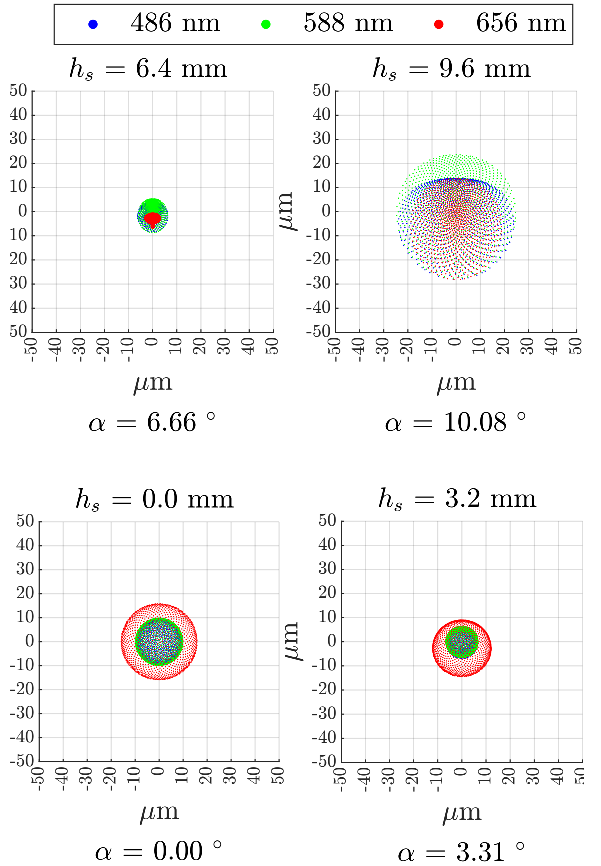

Fig. 10: Spot diagram of the model reported in Figures 9a and 9b at f/2.8 aperture for a 25-mm objective.

TABLE III: RMS radius of the spot diagram as a function of the detector position for the model reported in Figure 9

Camera Setup	Position on the screen [mm]	Position on the detector [mm]	Position in the FoV [deg]	RMS radius [μm]
25-mm objective	0	0	0	10.38
	3.2	1.45	3.31	7.71
	6.4	2.91	6.6	5.04
	9.6	4.41	10.07	17.34
50-mm objective	0	0	0	12.04
	3.2	1.47	1.69	11.82
	6.4	2.94	3.37	12.61
	9.6	4.41	5.05	17.59

Note that the above conditions were studied for narrow and wide FoV to ensure acceptable optical performance for the two extremal cases of the facility design. The final solution is shown in Figures 9a and 9b for wide and narrow FoVs and it is composed of 5 lenses. For the sake of completeness, the Zemax optimized model is provided as supplementary material of this paper. In particular, the collimating lens is composed of two lenses generating an equivalent focal length of 86.8 mm and the relay lens is composed of three lenses with an equivalent focal length of 82.8 mm. The optical performance of the final design is assessed by studying the RETINA spot diagram for different objective focal lengths at f/2.8. Note that this value of the aperture is selected as it is consistent with star tracker typical values and as larger apertures are usually associated with larger aberrations and distortions. The spot diagrams are reported for three wavelengths in Figures 10 and 11 for 25-mm and 50-mm objectives respectively.

The performance is strongly improved when compared with the simulations reported in Table II. Clearly, the performance degrades by increasing the angular distance

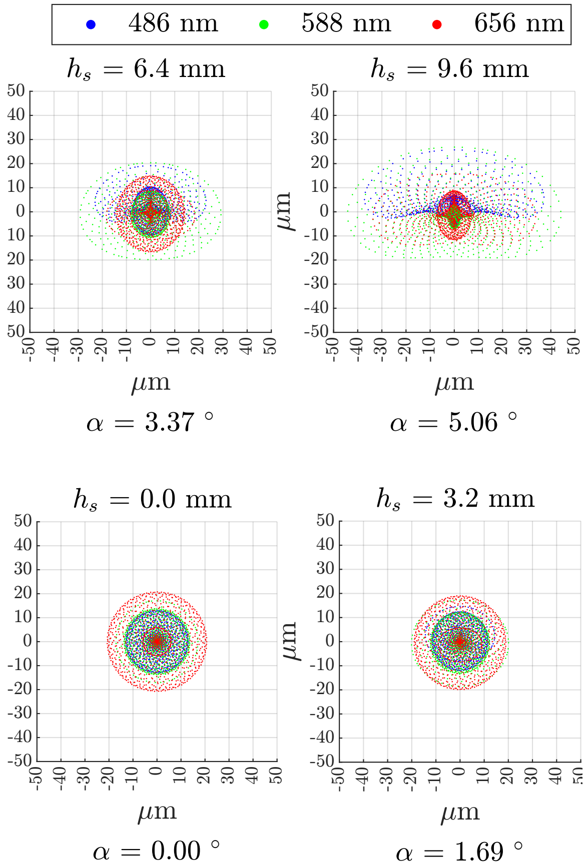

Fig. 11: Spot diagram of the model reported in Figures 9a and 9b at f/2.8 aperture for a 50-mm objective.

with respect to the boresight for both considered objectives, but the influence of distortions and aberrations remains limited. In particular, Table III underlines that the spot diagram is below the usual size of a single pixel, implying that light coming from a single point on the screen would be collected by a single pixel in the camera. An example of an image taken with the low-aberration setup is reported in Figure 12. The optical performance is largely improved when comparing it with Figure 8, implying precise stimulation of the camera along all its fields of view.

As the facility is designed taking only into account the camera FoV, a study is performed to understand which camera focal lengths f_{cam} and the camera diagonal sizes h_d can be used in the facility. This defines the envelope of camera characteristics that can tested. Moreover, to assess the quality of the stimulation for each camera, the following optical performance index is introduced:

$$L_{\%}^{\max} = 100 \max\left(\frac{r_r}{R_r}, \frac{r_c}{R_c}\right) \tag{14}$$

This index gives information about the quality of the stimulation when a camera is mounted in the facility. To quantify it, the highest crossing of the extremal ray cast in the vignetting analysis is used. Indeed, the optical performance of a lens system degrades when rays pass at the edges of a lens. This is because the paraxial hypothesis is less valid in this area leading to higher aberrations and distortions (see Figures 10 and 11 or Table III). Therefore, the higher $L_{\%}^{\max}$ is, the more the optical performance is degraded. It is worth noting that optical degradation does not imply that the image cannot be used for navigation thanks to the low-aberration design methodology presented in this work. The degradation is evaluated with respect to the nominal performance that is computed in the best conditions possible (i.e., the optical ray passing at the center of all lenses). Figure 14 shows the envelope of the camera characteristics parameters along with the optical performance index considering a camera with F#=2.8. Vertical dashed lines are associated with standard sensor diagonal size for space and Earth detectors, while purple lines denote the camera FoVs.

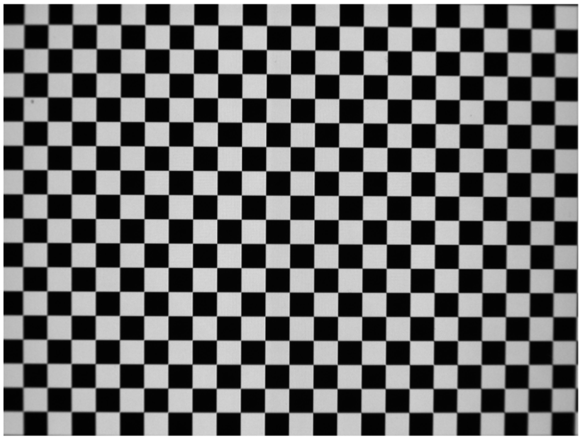

Fig. 12: An image of a regular pattern acquired in RETINA with the low-aberration configuration.

VI. Optical Facility Geometrical Calibration

To correctly stimulate the camera, the facility must be able to correctly project and reproduce the observed scene as in orbit. In theory, this can be achieved by limiting the lens distortions and aberrations, by centering and aligning the facility components. In practice, lenses induce distortions and aberrations errors to be cleaned out to ensure trustworthy stimulation. This error removal is essential as errors in the observed scene prevent the algorithm validation and characterization. A calibration procedure is required to characterize the facility's geometrical errors and to compensate them at software level [5].

A. Facility Projection Model

To estimate the facility's geometrical errors, it is necessary to establish a projection model for error quantification and compensation. In general, the goal of this section is to gather a projection model ensuring equivalence between the lines of sight (LoSes) observed in the facility and the ones generated in the rendering engine [27]. This procedure is detailed in Panicucci and Topputo [27] and a summary is provided here for the sake of completeness.

An overview of the stimulation workflow is presented in Figure 13. In the following, it is assumed in the projection model that the camera mounted in the facility is already calibrated. As the distortions and intrinsic camera matrix are known, it is possible to gather undistorted homogeneous LoSes from distorted pixel coordinates. It is then necessary to establish a mapping from the 3D virtual world to the screen image in order to determine the facility error model. Once these two contributions are established, it is possible to devise a calibration procedure to estimate the facility errors.

Let $\mathbb{S} = \{S,\, \boldsymbol{S}_1,\, \boldsymbol{S}_2\}$ and $\mathbb{F} = \{F,\, \boldsymbol{F}_1,\, \boldsymbol{F}_2\}$ be the 2D reference frames associated with the screen and facility images, respectively. Let $\mathcal{S} = \{s,\, \boldsymbol{s}_1,\, \boldsymbol{s}_2,\, \boldsymbol{s}_3\}$ and $\mathcal{F} = \{f,\, \boldsymbol{f}_1,\, \boldsymbol{f}_2,\, \boldsymbol{f}_3\}$ be the 3D reference frames associated with the screen and facility cameras, respectively. The projection from the 3D virtual world to the screen image can be represented by a linear projection matrix $[K_s]$ associated with the screen camera (i.e., the camera that generates via a rendering tool the images displayed on the screen). The screen camera projection matrix $[K_s]$ is expressed as follows:

$$[K_s] = \begin{bmatrix} f_{s_1} & 0 & c_{s_1} \\ 0 & f_{s_2} & c_{s_2} \\ 0 & 0 & 1 \end{bmatrix} \tag{15}$$

where f_{s_x} and f_{s_y} are the focal lengths in pixel units for the $\boldsymbol{S}_1$ and $\boldsymbol{S}_2$ directions, and c_{s_x} and c_{s_y} are the optical center coordinates in pixel units for the $\boldsymbol{S}_1$ and $\boldsymbol{S}_2$ directions. The components of $[K_s]$ are set as follows:

1) The optical center location $\boldsymbol{C}_s = (c_{s_1},\, c_{s_2})^T$ is coincident to the screen image center
2) The focal lengths f_{s_x} and f_{s_y} are set by noting that the smallest among the vertical and the horizontal FoVs must observe the vertical or the horizontal screen dimensions throughout the two-lens systems without cropping the image or observing the screen support. This implies that the screen camera must have the same FoV as the camera in the facility, but the screen resolution must be imposed to avoid errors when displaying the image.

Note that the projection model from the 3D virtual world to the screen does not account for any distortion or misalignment among the facility components.

Let $\mathfrak{F}$ be the facility camera projection model that maps the non-homogeneous 3D point to the non-homogeneous distorted 2D point:

$$^{\mathbb{F}}\boldsymbol{P}_d = \mathfrak{F}\left(^{\mathcal{F}}\boldsymbol{p}\right) \tag{16}$$

where $^{\mathbb{F}}\boldsymbol{P}_d$ is the non-homogeneous distorted 2D point expressed in the facility image reference frame $\mathbb{F}$ and $^{\mathcal{F}}\boldsymbol{p}$ is the non-homogeneous 3D points expressed the facility camera reference frame $\mathcal{F}$.

In the case of a pinhole camera model, a fundamental property of this model is that it must represent a projection, thus it must be scale-invariant. Therefore, for all scale k:

$$\mathfrak{F}\left(^{\mathcal{F}}\boldsymbol{p}\right) = \mathfrak{F}\left(k\, ^{\mathcal{F}}\boldsymbol{p}\right) \tag{17}$$

Finally, let $\mathfrak{D}$ be the error model that represents the facility distortions and misalignment errors. In detail, $\mathfrak{D}$ maps the warping from undistorted LoSes (i.e. the LoS modeling a rendering ray) to the LoSes as observed by the facility camera when distorted by the stimulation. Thus:

$$^{\mathcal{F}}\boldsymbol{\ell}_d = \mathfrak{D}\left(^{\mathcal{S}}\boldsymbol{\ell},\, \boldsymbol{\beta}\right) \tag{18}$$

$$^{\mathcal{S}}\boldsymbol{\ell} = \mathfrak{D}^{-1}\left(^{\mathcal{F}}\boldsymbol{\ell}_d,\, \boldsymbol{\gamma}\right) \tag{19}$$

where $\boldsymbol{\beta}$ and $\boldsymbol{\gamma}$ are sets of parameters used to model distortions and misalignment, $^{\mathcal{S}}\boldsymbol{\ell}$ is the undistorted LoS in the screen camera reference frame $\mathcal{S}$, and $^{\mathcal{F}}\boldsymbol{\ell}_d$ is the distorted LoS in the facility camera reference frame $\mathcal{F}$. Note that it is important to scale the LoSes such that $^{\mathcal{S}}\boldsymbol{\ell}^T \boldsymbol{s}_3 = {}^{\mathcal{F}}\boldsymbol{\ell}_d^T \boldsymbol{f}_3 = 1$. Similarly to Panicucci and Topputo [27], a polynomial model is used to parametrize the error model $\mathfrak{D}$ and its inverse.

By defining $^{\mathcal{F}}x_d = \boldsymbol{f}_1^T\, {}^{\mathcal{F}}\boldsymbol{\ell}_d$, $^{\mathcal{F}}y_d = \boldsymbol{f}_2^T\, {}^{\mathcal{F}}\boldsymbol{\ell}_d$, $^{\mathcal{F}}z_d = \boldsymbol{f}_3^T\, {}^{\mathcal{F}}\boldsymbol{\ell}_d$, $^{\mathcal{S}}x = \boldsymbol{s}_1^T\, {}^{\mathcal{S}}\boldsymbol{\ell}$, $^{\mathcal{S}}y = \boldsymbol{s}_2^T\, {}^{\mathcal{S}}\boldsymbol{\ell}$, and $^{\mathcal{S}}z = \boldsymbol{s}_3^T\, {}^{\mathcal{S}}\boldsymbol{\ell}$, the two models can be expressed in components:

$$^{\mathcal{F}}x_d = \sum_{k=0}^{N} \sum_{l=0}^{k} a_{(k-l),\, l}\; ^{\mathcal{S}}x^{(k-l)}\; ^{\mathcal{S}}y^{l} \tag{20}$$

$$^{\mathcal{F}}y_d = \sum_{k=0}^{N} \sum_{l=0}^{k} b_{(k-l),\, l}\; ^{\mathcal{S}}x^{(k-l)}\; ^{\mathcal{S}}y^{l} \tag{21}$$

$$^{\mathcal{S}}x = \sum_{k=0}^{N} \sum_{l=0}^{k} c_{(k-l),\, l}\; ^{\mathcal{F}}x_d^{(k-l)}\; ^{\mathcal{F}}y_d^{l} \tag{22}$$

$$^{\mathcal{S}}y = \sum_{k=0}^{N} \sum_{l=0}^{k} d_{(k-l),\, l}\; ^{\mathcal{F}}x_d^{(k-l)}\; ^{\mathcal{F}}y_d^{l} \tag{23}$$

$$^{\mathcal{S}}z = {}^{\mathcal{F}}z_d = 1 \tag{24}$$

where N is the maximum degree of the distortion model. For the sake of completeness, it is worth noting that $\boldsymbol{\beta}$ is the vector composed of the coefficients $a_{(k-l),\, l}$ and $b_{(k-l),\, l}$, while $\boldsymbol{\gamma}$ contains the coefficients $c_{(k-l),\, l}$ and $d_{(k-l),\, l}$. The relationship among the different distortion models is reported in Figure 15 for the sake of clarity.

When a screen image is displayed in the facility, the LoSes in the 3D virtual world are warped by the facility lenses. These warped LoSes are then projected in the facility camera obtaining the facility image. As the stimulation in the facility implies the warping of the scene, the camera in the facility observes a wrong fictitious world. Therefore, it is of primary importance to estimate the HIL-induced errors modeled with the mapping $\mathfrak{D}$ to correctly validate VBN algorithms. To do so, a detailed calibration procedure is developed as reported in Section VI-B.

Once the calibration is performed, the facility error model $\mathfrak{D}$ can be used to compensate for the HIL error at the software level by artificially manipulating the image to ensure the equivalence between what is observed in the 3D virtual world and what is observed by the facility camera. In a formal, way this procedure ensures that [27]:

$$^{\mathcal{F}}\boldsymbol{\ell} \simeq {}^{\mathcal{S}}\boldsymbol{\ell} \tag{25}$$

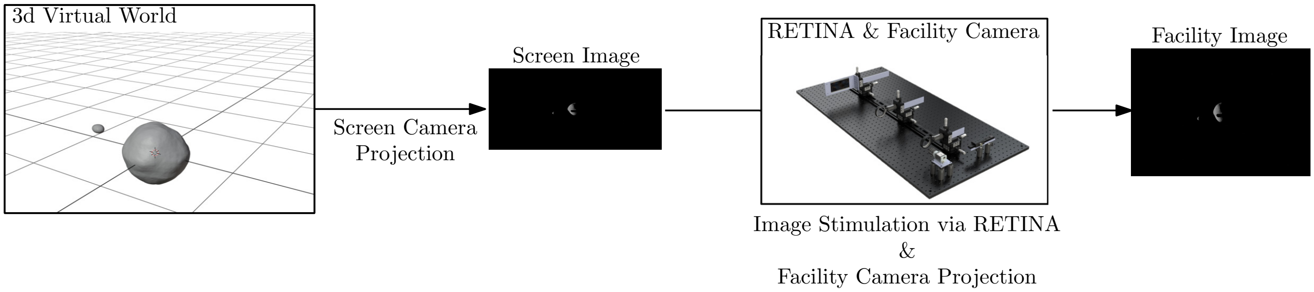

Fig. 13: The RETINA workflow from the 3D virtual environment to the image acquired in the facility.

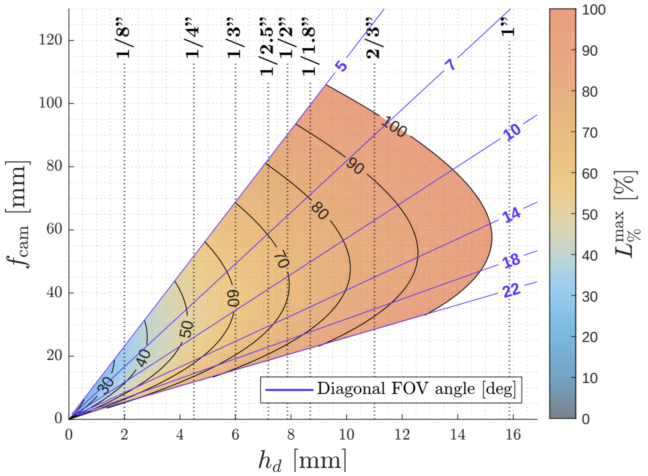

Fig. 14: The envelope of cameras that can be accommodated in the facility along with the optical performance index for each camera.

The compensation of HIL-induced error estimated in the calibration can be performed before and after the stimulation. If the compensation is performed before the stimulation (i.e. before displaying the image in the facility), the compensation is called upstream. Conversely, if the compensation is performed after the stimulation (i.e., after the facility camera acquisition), the compensation is called downstream. Panicucci and Topputo [27] shows that both compensations implies Equation 25. The selection of the most suitable procedure between the two strongly depends on the available rendering software, the hardware-in-the-loop setup, and the simulated scenario. Moreover, for unresolved objects (e.g., stars and planets) the upstream compensation can be complemented with a subpixel correction to achieve subpixel precision below the angular size of the screen pixel as observed by the camera. This subpixel compensation is presented in Section VI-C after having presented the calibration procedure in Section VI-B. In this paper, the upstream calibration is the only one employed between the two available in Panicucci and Topputo [27]. The upstream calibration functional workflow is reported in Figure 16 for the sake of completeness.

B. Calibration Procedure

The geometric calibration is in charge of estimating the coefficients $\boldsymbol{\gamma}$ and $\boldsymbol{\beta}$ to determine the error model $\mathfrak{D}$ and its inverse. The calibration procedure can be summarized as follows:

1) The facility is adjusted manually in an iterative procedure to center and align the different components independently. This ensures that rays from the screen pass as close as possible to the central part of the lenses, leading to reduced distortions and aberrations.
2) A series of calibration patterns composed of pixel-wise dots are projected on the screen and a series of images are acquired by the camera mounted in the facility. Pixel-wise dot patterns are preferred over other calibration patterns (e.g., checkerboard) because of their simplicity in the pattern generation pipeline and the accuracy of centroiding algorithms in detecting the pattern points.
3) The LoS detected by the camera are compared with the ones used to generate the image displayed on the screen. By minimizing the error between the two LoS sets, $\boldsymbol{\gamma}$ and $\boldsymbol{\beta}$ are estimated.

In more detail, the screen LoSes can be computed from the images displayed on the screen by knowing where the bright pixels are:

$$ {}^{\mathcal{S}}\boldsymbol{\ell} \propto [K_s]^{-1}\,{}^{\mathbb{S}}_{h}\boldsymbol{P} \tag{26} $$

where ${}^{\mathbb{S}}_{h}\boldsymbol{P}$ is a homogeneous point expressed in the screen image reference frame. Note that $\propto$ is used as ${}^{\mathcal{S}}\boldsymbol{\ell}$ must be scaled to ensure ${}^{\mathcal{S}}\boldsymbol{\ell}^{T}\boldsymbol{s}_3 = 1$. Analogously, the camera LoSes are gathered from extracted centroids in facility images:

$$ {}^{\mathcal{F}}\boldsymbol{\ell}_d \propto \mathfrak{F}^{-1}\left({}^{\mathbb{F}}\boldsymbol{P}_d\right) \tag{27} $$

where ${}^{\mathbb{F}}_{h}\boldsymbol{P}_d$ is a distorted non-homogeneous point expressed in the screen image reference frame. The coefficients are estimated by minimizing the residual errors between the screen LoSes and the camera LoSes. Thus:

$$ \hat{\boldsymbol{\beta}} = \arg\min_{\boldsymbol{\beta}} \left(\sum_{i=1}^{N_p} \left|\left| \mathfrak{D}\left({}^{\mathcal{S}}\boldsymbol{\ell}, \boldsymbol{\beta}\right) - {}^{\mathcal{F}}\boldsymbol{\ell}_d \right|\right| \right) \tag{28} $$

$$ \hat{\boldsymbol{\gamma}} = \arg\min_{\boldsymbol{\beta}} \left(\sum_{i=1}^{N_p} \left|\left| \mathfrak{D}^{-1}\left({}^{\mathcal{F}}\boldsymbol{\ell}_d, \boldsymbol{\gamma}\right) - {}^{\mathcal{S}}\boldsymbol{\ell} \right|\right| \right) \tag{29} $$

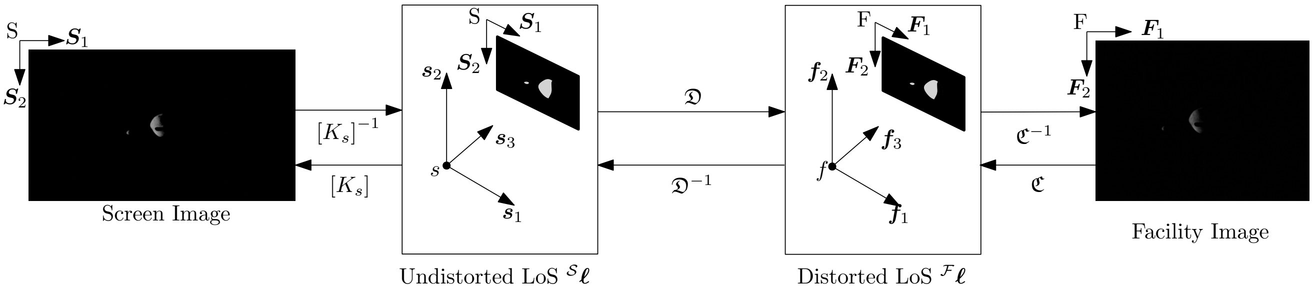

Fig. 15: The distortion models' relationship from the 3D virtual environment to the image acquired in the facility.

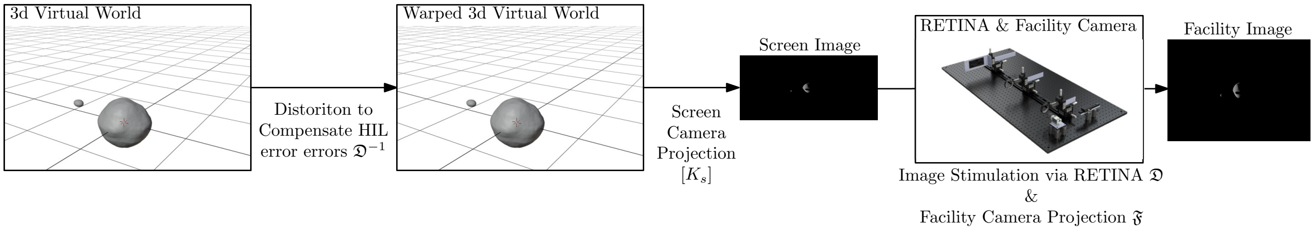

Fig. 16: The upstream compensation used to ensure the equivalence of the LoSes in the 3D virtual world with the ones detected by the camera.

where N_p is the number of calibration dots in all acquired images. By using a polynomial representation [27, 28, 20], the error model $\mathfrak{D}$ and its inverse are linear in the coefficients γ and $\boldsymbol{\beta}$, thus they are computed with linear least squares.

This procedure is reported hereunder for the RETINA facility to show the attainable performance on a physical system. For the sake of brevity, solely the results for the calibration of the inverse model error $\mathfrak{D}^{-1}\left({}^{\mathcal{F}}\boldsymbol{\ell}_d,\, \hat{\gamma}\right)$ are reported in this document as this is the one used for the upstream compensation. Note that numerical results are gathered with the wide-FoV camera configuration, using the 25 mm objective. The calibration procedure foresees the stimulation of the camera with point-wise patterns distributed such that they cover the full camera FoV. Then the points are associated and the optimization is performed. The quality of the process is studied both on the calibration and compensation. In the first case, the estimation process is performed and the post-fit residuals are studied to understand the quality of the estimation. In the second case, the estimated parameters are used to compensate facility geometrical errors in never-observed patterns, computing the error between the true pattern and the observed one. This last simulation is important as it reproduces the error compensation exploited during HIL testing.

To understand the quality of the calibration and compensation process, two figures of merit are used. First, the angular error between the true screen LoS (i.e., ${}^{\mathcal{S}}\boldsymbol{\ell}$) and camera LoS undisorted exploiting the estimated coefficients (i.e., $\mathfrak{D}^{-1}\left({}^{\mathcal{F}}\boldsymbol{\ell}_d,\, \hat{\gamma}\right)$). Second, the pixel error between the true screen LoS projected on the facility camera (i.e., $[K_f]{}^{\mathcal{S}}\boldsymbol{\ell}$ in non-homogeneous coordinates) and the undistorted camera LoSes projected on the facility camera (i.e., $\mathfrak{F}\left(\mathfrak{D}^{-1}\left({}^{\mathcal{F}}\boldsymbol{\ell}_d,\, \hat{\gamma}\right)\right)$ in non-homogeneous coordinates). This second figure of merit is used as it provides performance about the geometrical distribution on the image plane of the error between the two LoSes and gives insight into possible estimation biases. All results concerning calibration and compensation are obtained considering a camera with a 25-mm objective, sensor size of 1/1.8 inches, and F# of 2.8. This is because this camera has the worst calibration and compensation performance for the camera envelope reported in Figure 14, given the lower angular resolution of the pixel.

The angular post-fit residuals Probability Density Function (PDF) and Cumulative Density Function (CDF) for the calibration are depicted in Figure 17a. The angular error underlines that more than 99% of the points are below 5 arcseconds during calibration, leading to the correct estimation of the distortions and misalignment among the hardware components. In the figure, the two Instantaneous FoVs (IFoVs) are reported: the camera and the screen IFoVs. Note that the screen iFoV is the screen pixel angular size as seen by the camera in the facility. The results show that the post-fit residuals are smaller than the camera IFoV, thus the errors are within the camera pixel. These are also below the screen IFoV, indicating that the fitting process is well performed. This is confirmed by the 2D PDF associated with the post-fit residual pixel error which is reported in Figure 17b. The 2D pixel error is contained within the camera pixel with a mean close to zero, indicating an unbiased solution. Only some points experience a higher error, but they are limited in number and probably at the image border. Moreover, the 2D PDF is overall consistent with a zero-mean Gaussian PDF, as expected by a least-squares approach. This analysis concludes that the facility error model parameters are well-estimated with well-distributed post-fit residuals.

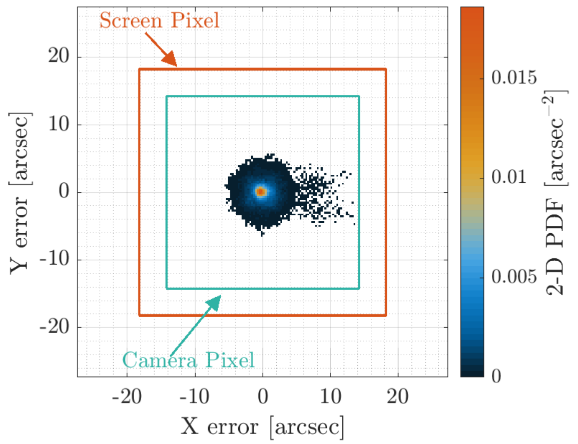

(a) Probability Density Function and Cumulative Density Function of the angular error.

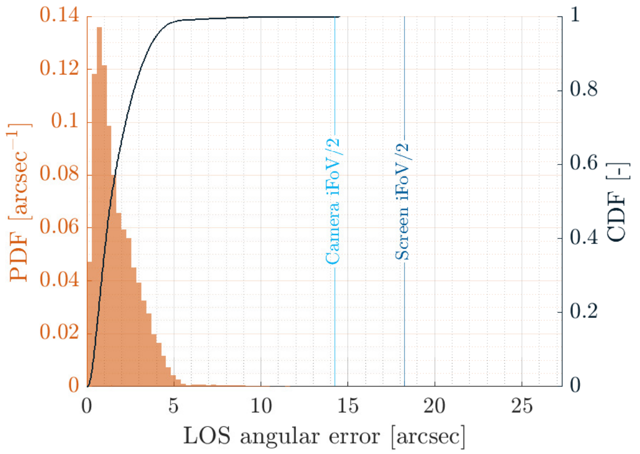

(b) Two-dimensional Probability Density Function of the pixel error.

Fig. 17: Results for the calibration.

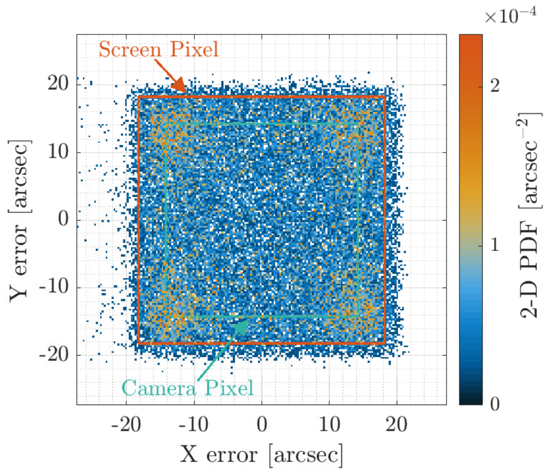

(a) Probability Density Function and Cumulative Density Function of the angular error.

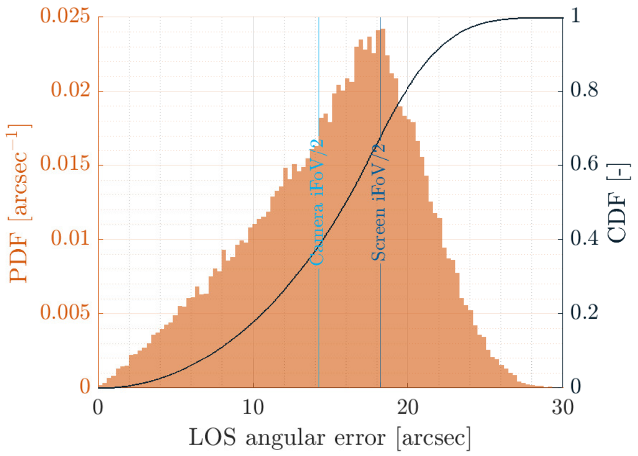

(b) Two-dimensional Probability Density Function of the pixel error.

Fig. 18: Results for the compensation.

Once the calibration is performed, the estimated parameters can be used to compensate for the HIL-induced errors. The compensation is thus tested on point-wise patterns never observed by the camera and not used for the calibration. As reported in Figure 16, the screen LoSes used to generate the point-wise patterns are firstly distorted exploiting the estimated error model. Then, the screen image of the pattern is generated, displayed on the screen, and acquired by the camera. Finally, the angular error and the 2D pixel error between the original screen LoSes (i.e., before the warping procedure) and the camera LoSes are computed. The results obtained with this procedure are reported in Figures 18a and 18b for the angular and pixel errors, respectively. The angular error PDF and CDF show that most of the observed points are displayed with an accuracy higher than the screen IFoV. This is also consistent with the 2D PDF associated with the pixel error. In this case, the PDF mean is close to zero, but it is not a Gaussian PDF. Indeed, as reported in Panicucci and Topputo [27], this PDF is consistent with a uniform PDF whose support is the screen pixel. This is compliant with the fact that the smallest portion of the screen to be illuminated is a screen pixel. Thus, when illuminating a single pixel, the error bounds cannot be reduced below the screen pixel boundaries. Nevertheless, this analysis shows that the upstream compensation allows stimulating the camera by reproducing the desired scene with an accuracy compliant with the smallest IFoV in the facility (i.e., the screen IFoV for the selected camera).

C. Subpixel compensation

It is not uncommon that image processing algorithms can achieve subpixel accuracy thanks to contextual information provided by neighboring pixels. Conversely, the geometric accuracy reproduced in the facility is limited by the angular size of the screen pixel. In particular, when a single pixel is lit, a single LoS direction associated with the center of the pixel can be reproduced. This means that to test algorithm performance, it is necessary to use screen pixels with iFoVs comparable to the accuracy of the image processing. In the context of unresolved objects, these limitations can be overcome by illuminating multiple screen pixels to achieve subpixel-precision stimulation of the camera. For resolved objects, the proposed procedure cannot be exploited as the neighboring pixels are needed to reproduce the scene.

The proposed approach is based on the idea that neighboring pixels to the one that is lit can be switched on as well to move the LoS centroid on the camera detector, thus increasing the accuracy. In particular, for each object, three pixels are lit. The intensity of each pixel is computed to fulfill two criteria. First, the sum of the intensities shall match the intensity of the celestial object F_0. Second, the coordinates of the center of mass of the reproduced shape shall coincide with the intended screen object coordinates ${}^{\mathbb{S}}\boldsymbol{P}_0$. In practice, the problem can be stated as:

$$\begin{cases} F_0 = F_1 + F_2 + F_3 \\ F_0\,{}^{\mathbb{S}}\boldsymbol{P}_0 = F_1\,{}^{\mathbb{S}}\boldsymbol{P}_1 + F_2\,{}^{\mathbb{S}}\boldsymbol{P}_2 + F_3\,{}^{\mathbb{S}}\boldsymbol{P}_3 \end{cases} \tag{30}$$

where ${}^{\mathbb{S}}\boldsymbol{P}_i$ with $i \in [1, 2, 3]$ is the coordinates of the ith pixel center and F_i with $i \in [1, 2, 3]$ is the ith pixel intensity. The selection of which pixels to switch on is not trivial as it must guarantee that the problem is feasible and that solutions involve only positive values of intensities. Figure 19 shows an example of the selection logic for a given configuration. In Figure 19, Pixel 1 is the one whose center is closer to ${}^{\mathbb{S}}\boldsymbol{P}_0$. The remaining two are selected among the eight neighbors of Pixel 1. In particular, Pixels 2 and 3 are those for which the point ${}^{\mathbb{S}}\boldsymbol{P}_0$ is contained inside the triangle determined by the centers of the three pixels. With this selection logic, the system has always a feasible solution since the pixels are not aligned. Moreover, the solution for the three intensities has always positive values for $F_0 > 0$. In practice, for each pointwise object, the system is solved analytically to find the correct distribution of intensities. The analytical expression is not reported here for the sake of brevity, but it can be determined from Equation 30. These values are then converted into an associated digital count defined by the radiometric calibration of the facility knowing the screen calibration curve as explained in Ornati et al. [33] and Andreis et al. [30].

The effectiveness of the correction is shown in Figures 20a and 20b, reporting the accuracy of the compensation procedure using the proposed sub-pixel correction. In this case, the errors are considerably reduced as they are lower than 8 arcsec in 99 % of the cases. It is worth noting that the errors almost reach the limit determined by the calibration residuals shown in Figure 17a and 17b.

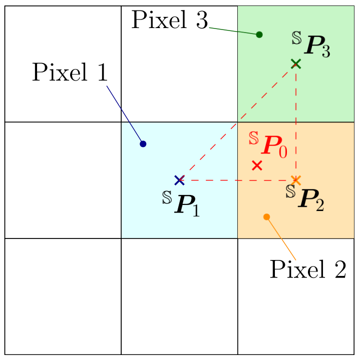

Fig. 19: Example of pixel selection logic for subpixel compensation correction.

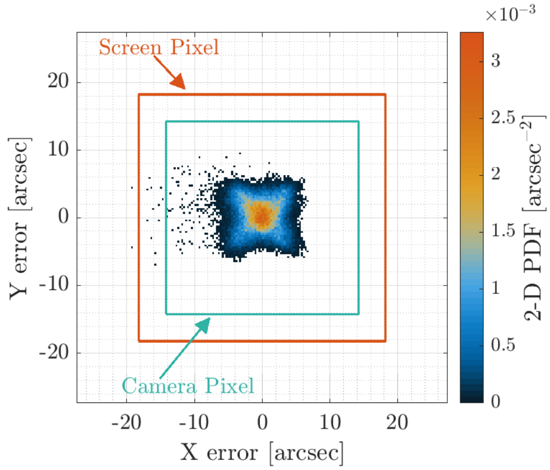

(a) Probability Density Function and Cumulative Density Function of the angular error for the compensation.

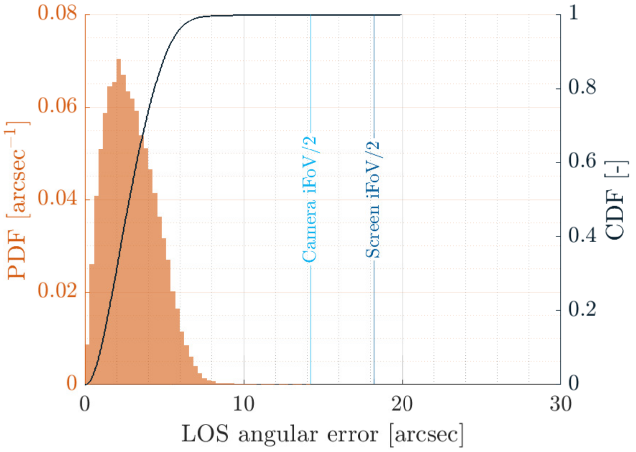

(b) Two-dimensional Probability Density Function of the pixel error for the compensation.

Fig. 20: Results for the subpixel compensation.

D. Sensitivity to External Temperature

As one of the purposes of optical stimulators is to perform long-lasting and extensive Monte Carlo simulations, it is of interest to characterize the facility behavior in time. According to the authors' expertise, the most impacting parameter on the calibration performance is external temperature. Moreover, this implicitly accounts for thermoelastic effects in the simulation which are hard to model in the rendering engine. Clearly, the thermostatic deformations experienced in the facility are not the ones affecting the camera in orbit, but the algorithm response to the presence of thermoelastic errors can give insight into the algorithm's robustness.

To understand the sensitivity of the estimated calibration to the temperature, a dedicated test is implemented to assess the stability of the calibration to temperature. The facility is calibrated at a given moment and calibration parameters are estimated and stored to be used during the test. Every minute, a series of unobserved patterns are projected on the screen using the upstream compensation. From the obtained centroids, the reprojection error is evaluated and the error mean and standard deviation for all the pattern points are computed. In the meanwhile, the temperature in RETINA is sampled via a temperature probe. Figure 21a shows the evolution of the mean calibration offset in time during the 28 hours of the experiment. Results show that the calibration is affected by the temperature variation as the optical elements of the facility are deformed and tilted by temperature gradients. While the calibration accuracy is affected by these effects, it is worth noting that the standard deviation of the calibration error remains constant in time, implying constant precision. Finally, to underline the correlation between calibration offsets and temperature variations, Figure 21b shows the temporal evolution of the temperature absolute derivative and the calibration shift derivative.

It is worth noting that it was decided not to compensate for these effects with a dedicated procedure as these are exactly the gaps that HIL simulations aim to represent when assessing the algorithm's robustness and performance.

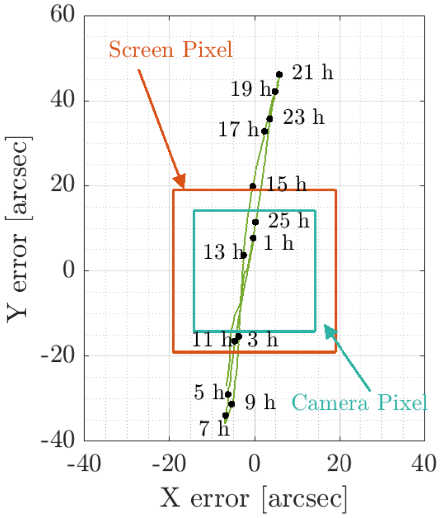

(a) Evolution of the calibration accuracy in time due to thermoelastic effects.

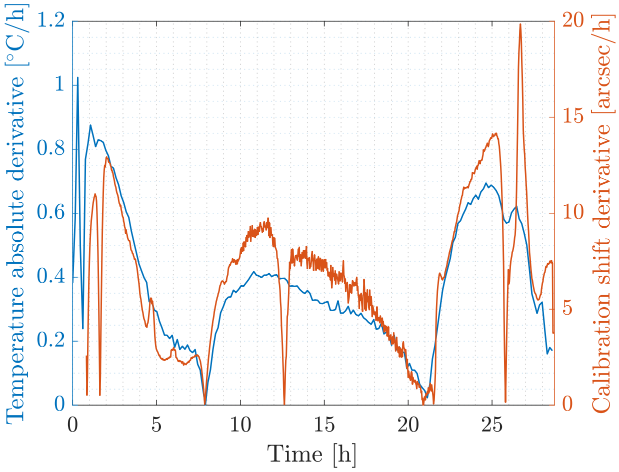

(b) Correlation between the room temperature derivative and the calibration accuracy shift derivative.

Fig. 21: Sensitivity of the calibration to the external temperature and thermoelastic effects.

VII. Applications

To show the applicability of the proposed low-accuracy variable-magnification optical stimulator to different scenes and hardware, two applications are presented. First, an attitude determination algorithm exploiting stars is outlined in Section VII-A. Second, an edge detection algorithm fitting the Moon limb is expounded. On the one side, the attitude determination algorithm is presented as the observed sources (i.e., the stars) are not resolved (i.e., their apparent size is smaller than one pixel). This implies that subpixel correction can be applied to locate accurately the star centroid in the camera images. Moreover, the camera used in this scenario uses a focal length of 25 mm with a sensor of 1/1.8 inches, leading to a diagonal full-cone FoV of 20 degrees. On the other side, the edge detection algorithm works with a resolved celestial object, thus the compensation can only achieve pixel accuracy. Nevertheless, this application shows the versatility of the geometrical calibration procedure. Indeed, the Moon is geometrically consistent with the associated space scene, despite the calibration having been performed using point-wise calibration patterns. Moreover, the camera used has a focal length of 50 mm with a sensor of 1/1.8 inches, leading to a diagonal full-cone FoV of 10 degrees.

A. Unresolved Targets: Attitude Determination

The first application is the attitude determination developed in the context of the EXTREMA project [38]. The proposed algorithm is a customization of the k-vector algorithm proposed by Mortari and Neta [39] bulked with the RANSAC algorithm [40]. The algorithm extracts bright spots in the image via a thresholding procedure and computes the associated centroids. Then, the registration between an onboard-stored star catalog is performed with the k-vector algorithm and the attitude is computed by solving the Wahba's problem. Note that the computed attitude solution robustness is increased by a consensus strategy based on RANSAC. More details about the algorithm can be found in Andreis et al. [3]. An example of the algorithm output is reported in Figure 22 where an image acquired in RETINA is shown in false color. In the figure, the red boxes are the identified stars with their associated star ID, while the blue boxes are the centroids not associated with any star.

The algorithm is tested on 1000 images generated with a dedicated rendering engine. Images are then compensated before displaying them on the screen as shown in Figure 16. The images are given as input to the attitude determination algorithm as taken by the camera. Finally, the algorithm output is compared against the available attitude truth.

Let $[BN]$ and $[\hat{B}N]$ be respectively the rotation matrices from the inertial reference frame $\mathcal{N}$ to the real and estimated body reference frames (i.e., $\mathcal{B}$ and $\hat{\mathcal{B}}$). To compare the two attitude solutions, the cross-boresight and the about-boresight errors are compared.

The cross-boresight error is computed as:

$$\phi = \text{acos}({}^{\mathcal{N}}\boldsymbol{b}_3^{T\,\mathcal{N}}\hat{\boldsymbol{b}}_3^{T}) \tag{31}$$

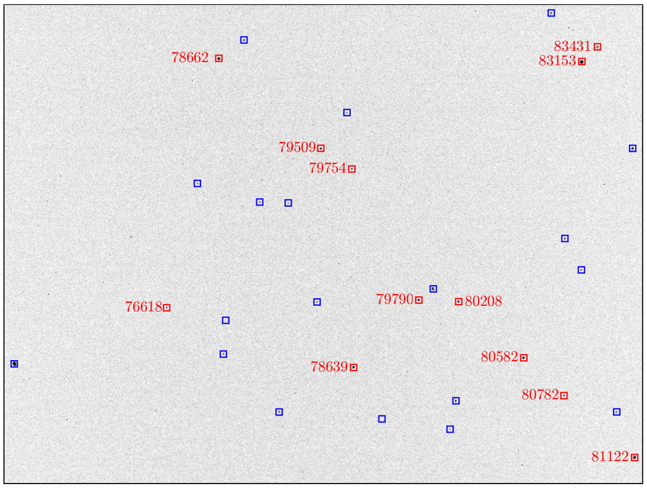

Fig. 22: Example of attitude determination on RETINA images.

where $\boldsymbol{b}_3$ and $\hat{\boldsymbol{b}}_3$ are the third unit vector of the $\mathcal{B}$ and $\hat{\mathcal{B}}$ reference frames, respectively. Note that the third unit vector is defined as the camera boresight in this work. This error represents the angle between the estimated camera boresight direction and the real one. It is worth noting that this error is related to the pitch and yaw estimation and, thus is mainly constrained by the camera and screen pixel sizes in HIL simulations [22, 17, 27]. Moreover, the about-boresight error is defined as:

$$\phi = \frac{\text{acos}({}^{\mathcal{N}}\boldsymbol{b}_1^{T\,\mathcal{N}}\hat{\boldsymbol{b}}_1^{T}) + \text{acos}({}^{\mathcal{N}}\boldsymbol{b}_2^{T\,\mathcal{N}}\hat{\boldsymbol{b}}_2^{T})}{2} \tag{32}$$

where $\boldsymbol{b}_1$ and $\boldsymbol{b}_2$, $\hat{\boldsymbol{b}}_1$ and $\hat{\boldsymbol{b}}_2$ are the first and second unit vectors of the $\mathcal{B}$ and $\hat{\mathcal{B}}$ reference frames, respectively. By definition, these two unit vectors are the ones lying on the image plane. This error is computed as the mean angular error of the axes laying on the image plane, thus it is directly related to the about-boresight angular error (i.e., the spacecraft roll). It is worth noting that this angle in a HIL simulation is not constrained only by camera and screen resolution, but also by the star asterisms recognized by the attitude determination algorithm [22, 17, 27].

The attitude is estimated in 97.2% of the cases which is consistent with software-in-the-loop simulations [41]. Among the remaining samples (i.e., 972), 1.03% has an attitude Absolute Knowledge Error (AKE) greater than 300 arcseconds, which is considered the limit for precise attitude determination. Moreover, Figures 23a and 23b show the cross-boresight and about-boresight errors as computed from the 1000 images. As expected, the cross-boresight angular solution is estimated with greater precision than the about-boresight one. It is worth noting that cross-boresight angular error is of the order of magnitude of the calibration error (see Figure 20a and 20b). Indeed, the main contributions to the cross-boresight angular solution are:

1) The precision in detecting the real centroids in camera images is usually around 0.3 pixels.
2) The precision in displaying a single star on the screen using the subpixel correction reported in Section VI-C.

On the contrary, the about-boresight angular solution is also influenced by the position of the identified stars in the image plane. Indeed, the closer the start to the camera cross-boresight, the higher the attitude error is. It is worth noting that in HIL optical facilities the stimulation is usually less accurate at the external part of the camera FoV (see Figure 10, Figure 11 and Table III). This is mainly because light passes in the external part of the lenses and it is keen to be more distorted and aberrated. Nevertheless, the about-boresight angular solution obtained in HIL simulations is consistent with state-of-the-art attitude determination algorithm performance. This can be achieved thanks to the optimized optical design and the subpixel compensation algorithm, allowing both precise stimulation of the camera.

B. Resolved Targets: Edge Detection

The second application relates to the detection of points belonging to the Moon limb from images de-

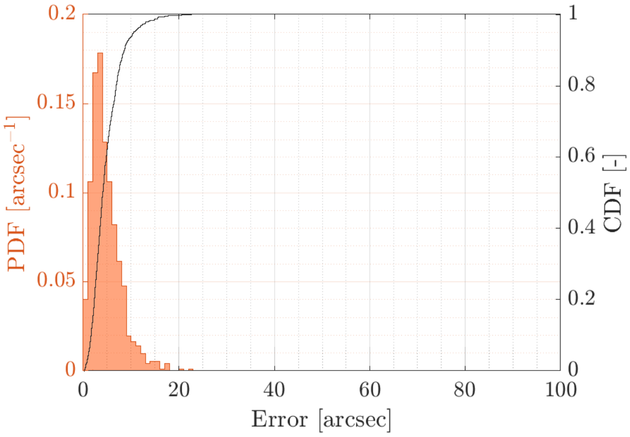

(a) Cross-boresight angular error.

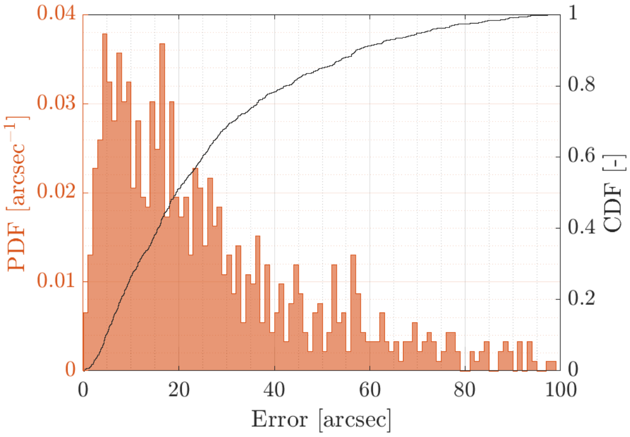

(b) About-boresight angular error.

Fig. 23: Probability Density Functions and Cumulative Density Functions of the attitude determination.

veloped in the context of LUMIO projects [34]. This application is of interest for two main reasons for this work. First, it enables facility validation with resolved objects where the compensation cannot be enhanced with subpixel correction. Thus, the accuracy of the optical observables is directly given by Figures 18a and 18b. For the developed facility, it is worth noting that the angular size of the screen pixel is larger than the one of the camera pixel (see Figures 18a and 18b). This is reflected in a less precise Moon limb stimulation.

Second, the geometrical calibration estimates the distortion coefficient by exploiting pointwise dots on the screen. The correct stimulation of the camera with a resolved celestial object is an independent validation of the geometrical calibration procedure and proof of its versatility. An example of the quality of the obtained stimulation is reported in Figure 24 where an image acquired in RETINA is shown along with the theoretical projection of the ellipsoid approximating the Moon. Figure 24 reports also a zoom on the edge to underline the accuracy obtained in the stimulation.

The acquired images are exploited to test a limb-based VBN algorithm. The proposed algorithm is inspired by the precursor work of Christian [42] and it is composed of several steps:

1) The image is scanned to identify a coarse estimation of points lying on the Moon's edge. The proposed scanning technique is implemented as reported in Panicucci et al. [34] to speed up the algorithm and avoid expensive calculations.
2) Patches of 7x7 pixels are extracted around the coarse edge location, and a first solution for the edge is found using the Laplacian of the Gaussian kernel. Then, this solution is refined at subpixel accuracy with the Zernike moment's method outlined in Christian [42].
3) Outliers are rejected using the RANSAC algorithm [40] fitting a circle on the found subpixel edge points.

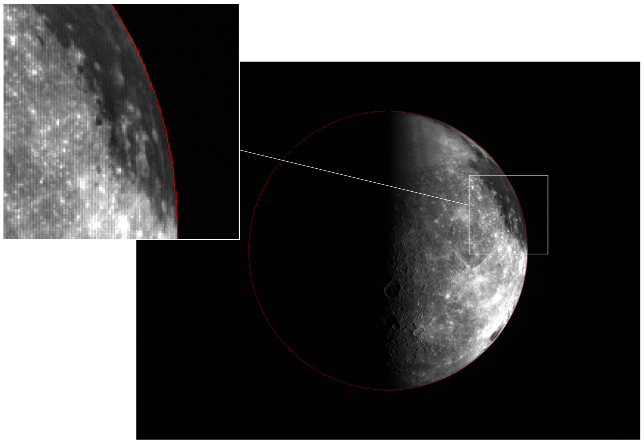

Fig. 24: An example of a Moon image acquired in RETINA with the theoretical Moon limb reported in red to show the geometrical consistency of the calibration.

This algorithm is tested on more than 4000 images of the first Nav&Eng cycle of the LUMIO trajectory [34]. The selected hardware is chosen to be as similar as possible to the LUMIO-Cam to increase the scenario representativeness in view of increasing the VBN algorithm TRL. Images are rendered offline and then compensated with the pixel upstream procedure. The acquired images are then given to the edge determination algorithm which provides three different sets of points: the coarse edge location, the subpixel edge location, and the inliers identified by the RANSAC. To compute the accuracy of the point set the radial error ϵ_r has been computed for each point with the following formula:

$$\epsilon_r = ||\boldsymbol{L}_{\text{edge}} - \boldsymbol{C}_{\text{Moon}}|| - r_{\text{Moon}} \tag{33}$$

where $\boldsymbol{L}_{\text{edge}}$ is the edge point location as estimated by the algorithm, while $\boldsymbol{C}_{\text{Moon}}$ and r_{Moon} are the true center and the true radius of the circle approximating the Moon projection.

An example of the edge detection output is reported in Figure 25. The Moon projection is reported in red, while the coarse limb points and the RANSAC inliers points are in blue and green, respectively. It is worth noting that some points, due to the scanning procedure, are also extracted on the terminator line, but are then rejected from the RANSAC algorithm. Moreover, it is possible to note that the RANSAC inliers points are qualitatively closer than the coarse edge location to the Moon projection.

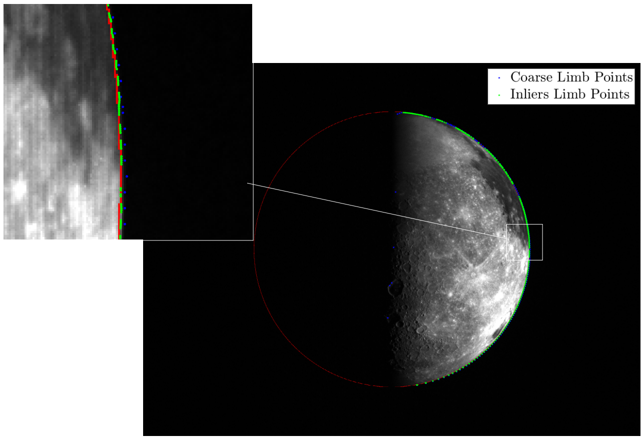

Fig. 25: An example of a Moon image acquired in RETINA reporting the points detected on the edge and the theoretical Moon limb.

This is also confirmed by the statistics of the radial error computed for all three point sets extracted from all the images of the LUMIO dataset. The PDFs and the CDFs for the three points sets are reported in Figures 26a and 26b respectively. It is worth noting that the refinement procedure works as expected also in HIL simulations, increasing the accuracy of the edge point location in the different algorithmic steps. Indeed, the coarse edge points are the most biased ones with a very high standard deviation. Then the subpixel correction step corrects the bias for the majority of the points, except for some outliers that are rejected effectively by the RANSAC. Indeed, the RANSAC inliers are an accurate solution of the limb location in the image with a reduced standard deviation and bias. Edge location performance is slightly worse than the simulations performed with synthetic images reported in Panicucci et al. [34], but this is mainly because the camera pixel is smaller than the screen pixel as observed by the camera.

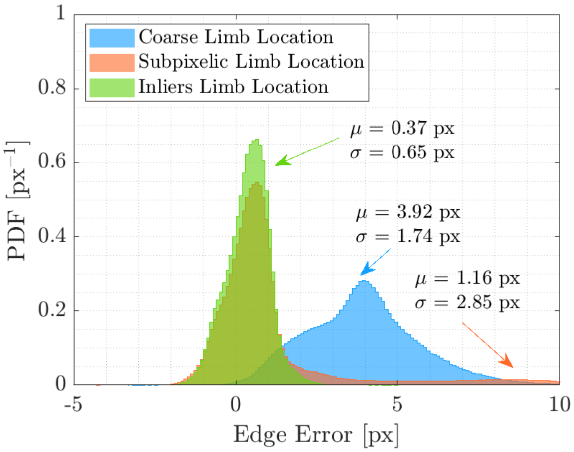

(a) Probability Density Functions.

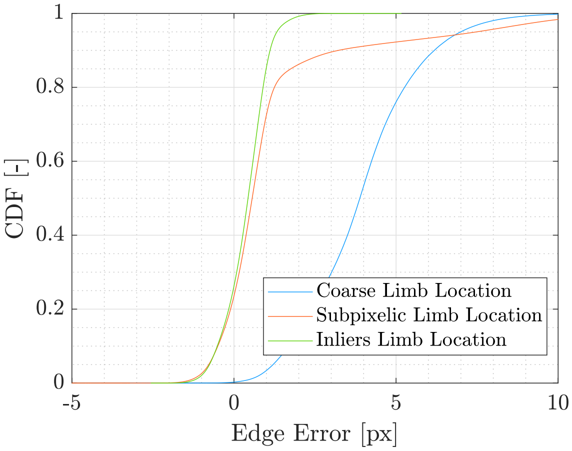

(b) Cumulative Density Functions

Fig. 26: Statistics of the edge detection steps for the different points extracted from the image.

VIII. Conclusion

This work presents a methodology to design and develop an optical stimualtor with low aberration and variable magnification. The methodology enables the fulfilling the design requirements and the identification of the facility components. The design drivers are analyzed taking into account the components accommodation in the facility and the vignetting due to the physical size of the lenses. An optical analysis underlines the presence of high distortions and aberrations for a two-lens optical stimulator, compromising the camera stimulation and its testing capacity. Therefore, a dedicated low-aberration design is performed using multiple lenses to reduce the facility distortions and aberrations. A geometrical calibration algorithm is also developed and discussed, enabling the estimation of the facility geometrical errors. This calibration model ensures an accurate stimulation of the camera during HIL testing.

A physical realization (i.e., RETINA) is presented to show an example of optical stimulators obtainable with the proposed methodology. The proposed approach led to the selection of the lens focal lengths and the facility integration. This results in a variable-magnification design, enabling the use of cameras with different fields of view, sensor sizes, and focal lengths. Once the facility is assembled, the designed calibration procedure is tested in RETINA. The compensation shows that a single point can be correctly observed by the camera with an accuracy

of less than 30 arcseconds for a pixel compensation and less than 10 arcseconds for a subpixel one. Moreover, the stability of the calibration to temperature variation is studied in a dedicated experiment. Results show that the calibration precision is immune to temperature variation, while its accuracy is impacted.
Finally, examples of RETINA applications are reported, to show the use of low-aberration optical stimulators. On the one hand, an attitude determination algorithm is tested to analyze the stimulation performance with a wide field of views, unresolved objects, and subpixel compensation. On the other hand, an edge detection algorithm is studied to underline the facility versatility to narrow the fields of view, resolved objects, and pixel compensation. Both applications underline that optical stimulators are crucial to test VBN and IP algorithms. These analyses are enabled by the design of an optical stimulator that exploits the methodology proposed in this paper. The proposed approach ensures the design of a versatile and accurate hardware-in-the-loop optical stimulator capable of handling different scenarios, various hardware, and heterogeneous celestial objects.

REFERENCES

[1] S. Bhaskaran, J. Riedel, S. Synnott, and T. Wang, "The deep space 1 autonomous navigation system-a post-flight analysis," in *Astrodynamics Specialist Conference*, 2000, p. 3935.

[2] E. Andreis, V. Franzese, and F. Topputo, "Onboard orbit determination for deep-space cubesats," *Journal of guidance, control, and dynamics*, vol. 45, no. 8, pp. 1466–1480, 2022.

[3] E. Andreis, P. Panicucci, and F. Topputo, "Autonomous vision-based algorithm for interplanetary navigation," *Journal of Guidance, Control, and Dynamics*, pp. 1–16, 2024.

[4] P. Panicucci, J. Lebreton, R. Brochard, E. Zenou, and M. Delpech, "Shadow-robust silhouette reconstruction for small-body applications," *Journal of Spacecraft and Rockets*, vol. 60, no. 3, pp. 812–828, 2023.

[5] P. Panicucci, "Autonomous vision-based navigation and shape reconstruction of an unknown asteroid during approach phase," Ph.D. dissertation, Toulouse, ISAE, 2021.

[6] P. Panicucci, J. Lebreton, R. Brochard, E. Zenou, and M. Delpech, "Vision-based estimation of small body rotational state," *Acta Astronautica*, vol. 213, pp. 177–196, 2023.

[7] P. Panicucci, F. Piccolo, S. Borgia, V. Franzese, and F. Topputo, "Current status of the lumio autonomous optical navigation experiment," in *12th International Conference on Guidance, Navigation & Control Systems (GNC)*, 2023, pp. 1–14.

[8] M. Pugliatti, V. Franzese, and F. Topputo, "Data-driven image processing for onboard optical navigation around a binary asteroid," *Journal of Spacecraft and Rockets*, vol. 59, no. 3, pp. 943–959, 2022.

[9] J. A. Christian, "A tutorial on horizon-based optical navigation and attitude determination with space imaging systems," *IEEE Access*, vol. 9, pp. 19 819–19 853, 2021.

[10] K. Dennison, N. Stacey, and S. D'Amico, "Autonomous asteroid characterization through nanosatellite swarming," *IEEE Transactions on Aerospace and Electronic Systems*, vol. 59, no. 4, pp. 4604–4624, 2023.

[11] C. Norman, C. Miller, R. Olds, C. Mario, E. Palmer, O. Barnouin, M. Daly, J. Weirich, J. Seabrook, C. Bennett *et al.*, "Autonomous navigation performance using natural feature tracking during the osiris-rex touch-and-go sample collection event," *The Planetary Science Journal*, vol. 3, no. 5, p. 101, 2022.

[12] B. Maass, S. Woicke, W. M. Oliveira, B. Razgus, and H. Krüger, "Crater navigation system for autonomous precision landing on the moon," *Journal of Guidance, Control, and Dynamics*, vol. 43, no. 8, pp. 1414–1431, 2020.

[13] R. Opromolla, G. Fasano, G. Rufino, and M. Grassi, "Pose estimation for spacecraft relative navigation using model-based algorithms," *IEEE Transactions on Aerospace and Electronic Systems*, vol. 53, no. 1, pp. 431–447, 2017.

[14] N. Rowell, S. Parkes, M. Dunstan, and O. Dubois-Matra, "PANGU: Virtual spacecraft image generation," in *5th Int. Conf. on Astrodynamics Tools and Techniques, ICATT*, 2012.

[15] J. Lebreton, R. Brochard, M. Baudry, G. Jonniaux, A. H. Salah, K. Kanani, M. Le Goff, A. Masson, N. Ollagnier, P. Panicucci, A. Proag, and C. Robin, "Image Simulation for Space Applications with the SurRender Software," in *Proceedings of the 11th International ESA Conference on Guidance, Navigation & Control Systems, 22 - 25 June 2021, Virtual*, 2021.

[16] J. Sola, "Quaternion kinematics for the error-state kalman filter," *arXiv preprint arXiv:1711.02508*, 2017.

[17] G. Rufino and A. Moccia, "Laboratory test system for performance evaluation of advanced star sensors," *Journal of Guidance, Control, and Dynamics*, vol. 25, no. 2, pp. 200–208, 2002.

[18] G. Rufino, D. Accardo, M. Grassi, G. Fasano, and U. Renga, A.and Tancredi, "Real-time hardware-in-the-loop tests of star tracker algorithms," *International Journal of Aerospace Engineering*, vol. 2013, pp. 1–13, 2013.

[19] N. Filipe, L. Jones-Wilson, S. Mohan, K. Lo, and W. Jones-Wilson, "Miniaturized star tracker stimulator for closed-loop testing of cubesats," *Journal of Guidance, Control, and Dynamics*, vol. 40, no. 12, pp. 3239–3246, 2017.

[20] M. A. Samaan, S. R. Steffes, and S. Theil, "Star tracker real-time hardware in the loop testing using

optical star simulator," *Spaceflight Mechanics*, vol. 140, 2011.

[21] V. Nardino, D. Guzzi, M. Burresi, M. Cecchi, T. Cecchi, F. Corti, M. Corti, E. Franci, G. Guidotti, I. Pippi, L. Salvadori, C. Spagnesi, and V. Raimondi, "MINISTAR: a miniaturized device for the test of star trackers," in *International Conference on Space Optics—ICSO 2018*, vol. 11180. SPIE, 2019, pp. 2821–2827.

[22] G. Rufino and A. Moccia, "Stellar scene simulation for indoor calibration of modern star trackers," *Space Technology*, vol. 21, no. 1, pp. 41–51, 2001.

[23] G. Rufino, D. Accardo *et al.*, "An effective procedure to test star tracker software routines using a sensor model," in *4th International Conference on Space Optics ICSO 2000*, 2000, pp. 703–712.

[24] D. Roessler, D. A. K. Pedersen, M. Benn, and J. L. Jørgensen, "Optical stimulator for vision-based sensors," *Advanced Optical Technologies*, vol. 3, no. 2, pp. 199–207, 2014.

[25] C. Beierle, J. Sullivan, and S. D'Amico, "Design and Utilization of the Stanford Vision-Based Navigation Testbed for Spacecraft Rendezvous," in *9th International Workshop on Satellite Constellations and Formation Flying, University of Colorado Boulder*, 2017.

[26] C. Beierle, J. Sullivan, and S. D'amico, "High-fidelity verification of vision-based sensors for inertial and far-range spaceborne navigation," in *26th International Symposium on Space Flight Dynamics (ISSFD)*, 2017.

[27] P. Panicucci and F. Topputo, "The TinyV3RSE Hardware-In-the-Loop vision-based navigation facility," *Sensors*, vol. 22, no. 23, p. 9333, 2022.

[28] C. Beierle and S. D'Amico, "Variable-magnification optical stimulator for training and validation of spaceborne vision-based navigation," *Journal of Spacecraft and Rockets*, vol. 56, no. 4, pp. 1060–1072, 2019.

[29] J. Kruger, A. W. Koenig, and S. D'Amico, "Starling formation-flying optical experiment (starfox): System design and preflight verification," *Journal of Spacecraft and Rockets*, vol. 60, no. 6, pp. 1755–1777, 2023.

[30] E. Andreis, P. Panicucci, F. Ornati, and F. Topputo, "Towards validation and verification of autonomous vision-based navigation for interplanetary spacecraft," in *12th International Conference on Guidance, Navigation & Control Systems (GNC)*, 2023, pp. 1–14.

[31] P. Panicucci, M. Pugliatti, V. Franzese, F. Topputo *et al.*, "Improvements and applications of the DART vision-based navigation test bench TinyV3RSE," in *44th AAS Guidance, Navigation and Control Conference*, 2022, pp. 1–19.

[32] M. Pugliatti, V. Franzese, P. Panicucci, and F. Topputo, "Tinyv3rse: The dart vision-based navigation test-bench," in *AIAA Scitech 2022 Forum*, 2022, p. 1193.

[33] F. Ornati, P. Panicucci, E. Andreis, and F. Topputo, "RETINA: a highly-versatile optical facility for camera-in-the-loop testing of spaceborne vision-based sensors," in *46th Annual AAS Guidance, Navigation and Control Conference*, 2024.

[34] P. Panicucci, F. Piccolo, A. Rizza, F. Topputo, and R. Walker, "Vision-based navigation for the lumio cubesat mission," in *46th Annual AAS Guidance, Navigation and Control Conference*, 2024.

[35] M. Pugliatti, F. Piccolo, A. Rizza, V. Franzese, and F. Topputo, "The vision-based guidance, navigation, and control system of hera's milani cubesat," *Acta Astronautica*, vol. 210, pp. 14–28, 2023.

[36] A. Madrid-Sánchez, J. Ortiz-Ocampo, C. Trujillo, and H. Ottevaere, "Off-the-shelf optical systems design enabled by an evolution strategy: front stop case," *Journal of Physics: Photonics*, vol. 6, no. 1, p. 015002, 2023.

[37] L. Ryzhikov, "Method for designing optical systems from the off-the-shelf optical components," in *Current Developments in Lens Design and Optical Engineering XXIII*, vol. 12217. SPIE, 2022, pp. 161–170.

[38] G. Di Domenico, E. Andreis, A. Carlo Morelli, G. Merisio, V. Franzese, C. Giordano, A. Morselli, P. Panicucci, F. Ferrari, and F. Topputo, "The erc-funded extrema project: Achieving self-driving interplanetary cubesats," in *Modeling and Optimization in Space Engineering: New Concepts and Approaches*. Springer, 2022, pp. 167–199.

[39] D. Mortari and B. Neta, "K-vector range searching techniques," *Adv. Astronaut. Sci*, vol. 105, no. 1, pp. 449–464, 2000.

[40] R. Hartley and A. Zisserman, *Multiple View Geometry in Computer Vision*, 2nd ed. Cambridge University Press 2000, UK, 2004, ch. 3, pp. 117–120.

[41] E. Andreis, H. Krüger, S. Woicke, P. Panicucci, and F. Topputo, "Hardware-in-the-loop validation of autonomous interplanetary navigation algorithms for interplanetary cruises with the optical star stimulator," in *AIAA Scitech 2024 Forum*, 2024, p. 0776.

[42] J. A. Christian, "Accurate planetary limb localization for image-based spacecraft navigation," *Journal of Spacecraft and Rockets*, vol. 54, no. 3, pp. 708–730, 2017.

Paolo Panicucci is an assistant professor of aerospace systems at Politecnico di Milano, Italy. His research is focused on spacecraft GNC, hardware-in-the-loop simulations, and the use of cameras for scientific purposes. He serves as PI or Co-PI in multiple projects funded by national and international sponsors. He is part of the science working group of NASA DART, ESA Hera, ESA RAMSES, and ESA LUMIO. He has published 16 peer-reviewed articles in international journals and over 80 works in total.

Fabio Ornati is a PhD student at Politecnico di Milano, Italy. He holds a MSc in Space Engineering from Politecnico di Milano. His research interests focus on the development of hardware-in-the-loop methodologies for testing autonomous guidance, navigation and control algorithms. His expertise covers camera simulation, camera calibration, image processing and computer vision.

Francesco Topputo is a full professor of aerospace systems with Politecnico di Milano, Italy, where he leads the Deep-Space Astrodynamics Research and Technology (DART) research team composed of 45 researchers. He has been Principal Investigator in numerous research projects. He has authored more than 100 journal articles and more than 300 works in total. His research interests include space flight dynamics and control, autonomous navigation, interplanetary CubeSat missions, and system design.